CHALMERS

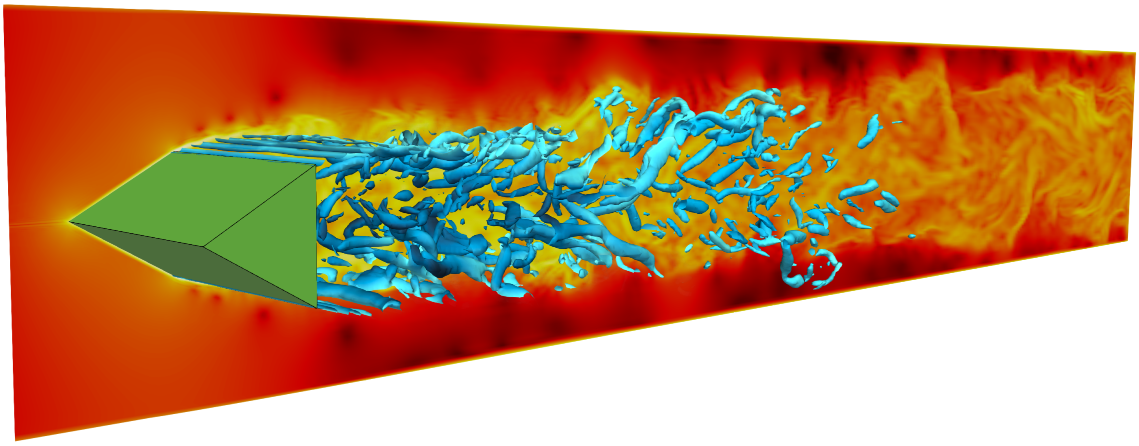

Large Eddy Simulation Techniques for Predicting Turbulent Combustion of Hydrogen Fuel

Master's thesis in Applied Mechanics

NICHOLAS OTWAY

Department of Mechanics and Maritime Sciences
CHALMERS UNIVERSITY OF TECHNOLOGY
Göteborg, Sweden 2020

MASTER'S THESIS IN APPLIED MECHANICS

Large Eddy Simulation Techniques for Predicting Turbulent Combustion of Hydrogen Fuel

NICHOLAS OTWAY

Department of Mechanics and Maritime Sciences
Division of Fluid Dynamics
CHALMERS UNIVERSITY OF TECHNOLOGY

Göteborg, Sweden 2020

Large Eddy Simulation Techniques for Predicting Turbulent Combustion of Hydrogen Fuel
NICHOLAS OTWAY

Master's thesis 2020:86
Department of Mechanics and Maritime Sciences
Division of Fluid Dynamics
Chalmers University of Technology
SE-412 96 Göteborg
Sweden
Telephone: +46 (0)31-772 1000

Cover:
Premixed turbulent combustion in a model combustor. The figure shows iso–surfaces of the second invariant of the velocity gradient tensor and a contour plot of the magnitude of the strain rate tensor.

Chalmers Reproservice
Göteborg, Sweden 2020

Large Eddy Simulation Techniques for Predicting Turbulent Combustion of Hydrogen Fuel
Master's thesis in Applied Mechanics
NICHOLAS OTWAY
Department of Mechanics and Maritime Sciences
Division of Fluid Dynamics
Chalmers University of Technology

ABSTRACT

The concept of a hydrogen economy has reified in recent times and many envision hydrogen to become the fuel of choice in the not–too–distant future. Whether it will be used for power generation, domestic heating, or vehicular propulsion, the benefits of hydrogen are well documented and highly desirable. This thesis investigates numerical methods currently used to study the turbulent combustion of conventional hydrocarbon–based fuels and how a similar framework can be applied to the special case of hydrogen combustion.

A discussion on the importance of seeking alternatives to current fuel sources is given. The case for adopting hydrogen as the preferred alternative is outlined, along with the challenges that must be overcome if we are to do so. The theoretical foundations of combustion theory presented, includes the relevant fundamental concepts from the fields of thermodynamics, chemical kinetics and turbulent flow. The procedure for constructing large eddy simulations for turbulent combustion systems is described. This procedure is used to build a model for propane combustion which is validated against experimental data.

In the absence of empirical validation data for hydrogen combustion, techniques are instead devised to adapt hydrogen into the working model for propane combustion. Certain quantities related to the flame speed and heat release of the propane case are used to estimate a specific setup configuration to be used for the hydrogen case. The goal is to configure the hydrogen case in such a way that the system will exhibit flame speed and heat release characteristics that are comparable the corresponding flame speed and heat release characteristics of the propane case. By designing the new hydrogen model in such a way that the flame speed and heat release characteristics are equivalent to those of the trusted propane model, a point of reference is available for which the two different systems can be compared and contrasted. The results obtained from each combustion model are presented followed by an evaluation of modelling strategy.

Keywords: Computational Fluid Dynamics, Large Eddy Simulation, Turbulent Combustion, Hydrogen, Propane, Fluent, Finite Rate Chemistry, Thickened Flame Model, AFRL Validation Rig

Preface

The control of fire was widespread during the Palaeolithic era and was essential to the survival and well–being of nomadic hunter–gatherers. Some of the most significant milestones along the timeline of recorded history can be largely attributed to innovations that relied on the combustion process as a means of harnessing energy. Stone tools became obsolete when the first metallurgists used primitive smelting techniques to extract and purify metals from ore deposits. Transportation changed forever once vehicles powered by steam replaced those on land driven by animals and those at sea driven by wind.

Combustion has been of great importance to the development of civilisation and it will continue to be. As in the past, the role it plays will continue to evolve according to the needs and desires of society. Almost every aspect of life today depends, in part, on our ability to generate energy by some means of combustion. In order to continue satisfying the increasing demand for energy, it must be generated, delivered and consumed in a responsible manner. In modern times, the overwhelming majority of energy consumption has been obtained by the burning of fossil fuels. It is indisputable that this is unsustainable and alternative sources of energy must therefore be found if we are to avoid disastrous consequences.

Nature has gifted us with an abundance of energy that exists in many forms and is readily available to us. Recent advances in wave, wind and solar, as well as continued innovations in hydro and nuclear power, will all play a part in securing our energy needs. Fossils fuels have been incredibly useful as an energy source and as an energy carrier. But the laissez–faire approach to anthropogenic greenhouse gas emissions does not feature in a future of clean and sustainable energy. Thankfully there are promising types of combustible fuels that do not have the same terrible effects on the environment. Hydrogen gas is one such example.

The widespread use of hydrogen as a fuel has been long anticipated [1][2][3]. Yesterday's vision of the hydrogen economy is today the subject of government strategies and roadmaps [4][5][6][7][8] that set 2030 and 2050 as key progress milestones. Government policy and timelines provide industry with the confidence to invest in new hydrogen fuel and hydrogen fuelled technologies [9][10][11][12][13][14].

However, there are considerable technical challenges remaining before it can be adopted on an industrial scale. An array of unanswered questions confront the research community, who are motivated to seek out solutions and satisfy their curiosity. The distinct nature of hydrogen gas, such as its high reactivity and diffusivity, make for atypical combustion dynamics compared to the burning of conventional hydrocarbons [15][16][17][18]. Since the H_2 molecule plays an active part in the combustion of all carbon–based fuels, a better understanding of its reaction characteristics and radical species kinetics, will also assist in the development of other alternative fuels, while guiding us towards a more eco–friendly use of regular fuels [19][20][21][22][22].

This thesis aims to contribute to the ongoing research in the field of hydrogen combustion, with the desire of making hydrogen fuel not just a feasible, but a desirable option in the quest for a sustainable energy future.

"Science can amuse and fascinate us all, but it is Engineering that changes the world."

- Isaac Asimov

Acknowledgements

I would like to give a very special thanks to my supervisor, Daniel Lindblad, whose enthusiasm and perspicacity has been a constant source of knowledge and inspiration. His friendly encouragement and astute guidance were always on offer and I'm grateful for all the time he invested in our frequent Zoom meetings, not to mention the countless number of emails we exchanged. I am particularly appreciative of the patience he showed whilst my productivity was brought to a halt by two shoulder operations. One could not have asked for a better supervisor than Daniel, who, in recognition of his fondness for German words, has been absolutely wunderbar! I would also like to thank my examiner, Niklas Andersson, for the feedback that he provided on my oral presentation and my thesis report.

Above all, I want to express my gratitude to my parents back home in Australia. Their endless support and encouragement were crucial to my success in Sweden. My mother's mastery of the English language combined with her eagle–eye for written mistakes is a cherished tool at my disposal. Her input is incredibly valuable when preparing important documents that warrant extra special attention, including this thesis. The regular, if not daily, Zoom conversations I had with my father whilst working on this project were a refreshing way to break up the long hours. Thanks to his infinite curiosity and enthusiasm, our discussions typically consisted of him quizzing me about the task I was working on and how I planned to solve any problems. It was always an enjoyable and much–needed social interaction that was otherwise lacking on account of working remotely due to the COVID situation. No doubt it also helped me to improve my understanding of complex topics by attempting to explain things in simpler terms. It wouldn't have been possible to accomplish so much without Mum and Dad. Thank you for everything.

NOMENCLATURE

Acronyms

AFRL	Air Force Research Laboratory
CFD	Computational fluid dynamics
CV	Control volume
FRC	Finite rate chemistry
GS	Grid scale
LES	Large eddy simulation
LHS	Left–hand side
NS	Navier–Stokes
RANS	Reynolds averaged Navier–Stokes
RHS	Right–hand side
RMS	Root mean square
SGS	Subgrid scale
TFM	Thickened flame model

Latin Symbols

A	Pre–exponential factor	s^{-1}
C_p	Heat capacity at constant pressure	$J\ kg^{-1}\ K^{-1}$
Da	Damköhler number	
$\mathcal{D}_{ik}$	Binary diffusion coefficient	$kg\ m^{-2}\ s^{-1}$
D	Mass diffusion coefficient	$m^2\ s^{-1}$
D_{th}	Thermal diffusivity	$m^2\ s^{-1}$
E	Total energy per unit mass	$J\ kg^{-1}$
E_A	Activation energy	$J\ mol^{-1}$
G	Gibbs free energy	J
$\Delta_r G$	Reaction Gibbs energy	$J\ mol^{-1}$
H	Total enthalpy	J
h	Total enthalpy per unit mass	$J\ kg^{-1}$
h_s	Sensible enthalpy	$J\ kg^{-1}$
Δh_f°	Enthalpy of formation	$J\ kg^{-1}$
I	Turbulence intensity	
K	Reaction rate constant	s^{-1}
Ka	Karlovitz number	
k	Turbulent kinetic energy	$m^2\ s^{-2}$
$\mathcal{L}$	Length scale	m
$\dot{m}$	Mass flow rate	$kg\ s^{-1}$
m	Mass	kg
n	Number of moles	mol
p	Pressure	$kg\ m^{-1}\ s^{-1}$
Q	Heat of combustion	$J\ kg^{-1}$
Re	Reynolds number	
R_u	Universal gas constant	$J\ mol^{-1}\ K^{-1}$

S	Total entropy	$\mathrm{J\ K^{-1}}$
s_L^0	Laminar flame speed	$\mathrm{m\ s^{-1}}$
T	Temperature	K
t	Time	s
$\mathcal{U}$	Velocity scale	$\mathrm{m\ s^{-1}}$
U_0	Mean free stream flow velocity	$\mathrm{m\ s^{-1}}$
u_i	Cartesian component of velocity vector	$\mathrm{m\ s^{-1}}$
W	Molecular weight	$\mathrm{g\ mol^{-1}}$
X	Mole fraction	
$[X]$	Molar concentration	$\mathrm{mol\ m^{-3}}$
x_i	Cartesian component of position vector	m
Y	Mass fraction	

Greek Symbols

Δ	Grid spacing	m
δ_{ij}	Kronecker delta	
δ_L^0	Laminar flame thickness	m
ε	Turbulent dissipation rate	$\mathrm{m^2\ s^{-3}}$
λ	Thermal conductivity	$\mathrm{J\ m^{-1}\ s^{-1}\ K^{-1}}$
μ	Dynamic viscosity	$\mathrm{kg\ m^{-1}\ s^{-1}}$
ν	Net species stoichiometric coefficient	
ν'	Reactant species stoichiometric coefficient	
ν''	Product species stoichiometric coefficient	
ξ	Reaction progress variable	
ρ	Density	$\mathrm{kg\ m^{-3}}$
τ_{ij}	Viscous stress tensor	$\mathrm{kg\ m^{-1}\ s^{-2}}$
τ_{ij}^{sgs}	Subgrid scale stress tensor	$\mathrm{kg\ m^{-1}\ s^{-2}}$
$\uptau_c$	Chemical timescale	s
$\uptau_t$	Integral timescale	s
$\uptau_\eta$	Kolmogorov timescale	s
υ	Chemical potential	$\mathrm{J\ mol^{-1}}$
ϕ	Equivalence ratio	
$\dot{\omega}$	Reaction rate	$\mathrm{kg\ m^{-3}\ s^{-1}}$

Miscellaneous

$\propto$	Directly proportional to
$\sim$	Scales according to
$\bar{f}$	Filtered quantity
f'	Perturbation with respect to filtered quantity
$\widetilde{f}$	Favre filtered quantity
f''	Perturbation with respect to Favre filtered quantity
$\langle f \rangle$	Time averaged quantity

CONTENTS

1 Introduction

1.1 Background

Combustion is a complex process. In simple terms it can be thought of as a process that combines a fuel with an oxidant to produce heat and light. Our current understanding of what we now know as combustion has its origins in the emergence of fire as a critical resource for human development, and as a vital resource for the comfort, if not survival, of individuals. Humanity's desire, perhaps existential need to understand fire, has been a journey begun with prayers and offerings to the earliest Fire Gods, and continued by generations of philosophers and scientists from ancient times along the way evolving the study of fire into what we call today the study of combustion.

Our ability to manipulate fire has facilitated the development of sophisticated technologies and led to revolutionary discoveries. Many of these triumphs would not have been possible without access to the energy that combustion provides. Today approximately 91% of the global supply of primary energy involves some form of combustion [23]. The energy obtained through combustion is put to use in countless ways. Whether heating water, generating electricity or launching satellites, combustion is an indispensable cog in the machine of society. It is just as important today as it has been for tens of thousands of years. Charles Darwin referred to the discovery of fire as "probably the greatest, excepting language, ever made by man"[24].

Although our modern machines and deeper understanding of combustion allows us to perform acts that would appear godlike to our ancestors, we are a very long way from deity status. Despite our impressive exploits, our perceived prowess will not always shield us from the dangers of playing with fire. We are now confronted by an ominous threat that is a direct result of what we have accomplished with combustion. The fossil fuels we burn to drive our vehicles and light our homes is causing great harm to our health [25][26] and to the environment [27][28][29]. Persistent use of hydrocarbon fuels is happening on an immense global scale, and pollutant products generated as a result of the combustion process are released into the atmosphere. Oxides of nitrogen, sulphur oxides, organic compounds and particulate matter are the most common pollutant substances [30].

Those working in combustion science are given the challenge of seeking out ways to reduce harmful emissions, improve fuel efficiency and enable increased use of alternative fuels with the ultimate aim of achieving large–scale, clean energy production. There are countless activities, occasions and functions that can only be feasibly performed at the present time with the burning of fossil fuels. This will remain so for the foreseeable future and combustion will still feature as the primary means of global energy production for decades to come.

The study of combustion modelling is essential if a successful and timely transition away from fossil fuels is to be achieved. Furthermore, combustion modelling has applications in a range of industries and is not exclusive to the energy and transport sectors. For example, the manufacturing process for pharmaceutical products and construction materials can require a high degree of temperature control. Ecological and fire prevention practices can also benefit from the predictive capability of combustion modelling.

The optimisation of existing technologies and the pursuit of innovative new designs, typically involves a substantial degree of numerical modelling to complement the theoretical and experimental aspects of research and development. With access to greater computational resources, scientists and engineers can generate sophisticated simulations by obtaining numerical solutions to large sets of equations that describe the underlying physics of a particular system. The numerical approach has proven to be highly successful for testing theoretical predictions. It also eases the burden on product developers who can optimise a virtual model before building costly physical prototypes.

1.2 Motivation

The societal need to phase out the burning fossil fuels is now widely accepted and the matter has progressed into a vehement discussion about the new types of fuel that should be used instead. Some potential replacements for fossil fuels are different types of biofuels [31]. Although carbon dioxide is emitted when biofuels are burnt, they are considered carbon–neutral as they are typically produced by agricultural means where atmospheric carbon dioxide is absorbed through photosynthesis. Another prominent alternative fuel is hydrogen gas, which is the focus of this thesis.

As a fuel, hydrogen gas has a lot of attractive qualities [32]. It is lightweight, energy dense, and carbon free. Ironically, the physical characteristics that make hydrogen so appealing also give rise to the complications associated with its use. For example, because it is the lightest element on the periodic table, hydrogen has a very low volumetric storage capacity and a high propensity for leakage. The substantial amount of energy that it releases makes hydrogen a more powerful propellant than regular hydrocarbons, but its rapid burning velocity also makes it more hazardous to work with. Hydrogen is the most abundant element in the universe, but its gaseous form is extremely rare on earth. Separating it from other substances can be a complex and costly process.

As a society, we are obligated to seek out cleaner forms of energy. Despite the difficulties with adopting hydrogen as a mainstream fuel, its advantages cannot be ignored and the benefits are therefore worth pursuing. We must ensure that we are equipped with the knowledge and the tools that are required to confront all of the challenges related to the availability, production, distribution, storage, safety and combustion of hydrogen gas.

1.3 Turbulent Combustion Modelling

Turbulent combustion modelling is an expansive topic that incorporates a range of different scientific disciplines. Broadly speaking it is a combination of thermodynamics, chemical kinetics and fluid mechanics. Date [33] defines combustion as “a phenomenon that involves the change in the chemical state of a substance from a fuel state to a product state via a chemical reaction accompanied by the release of heat energy”.

Thermodynamic equations of state are used to describe the composition of matter, its physical characteristics and the energy content within a system. For a particular region of space at any point in time, the extensive properties of an unburnt gas mixture will indicate if a combustion event is possible. Similarly, the same equations are used to compute the properties of the burnt gas mixture in its post–combustion state. However, the equations of state are not time dependant and can only provide information about the instantaneous state of the system before, during or after combustion. They do not, however, define the path between the reactants and the products.

A kinetic analysis is required to describe the transient aspect of the change from reactant to product, including the creation and destruction of short–lived intermediate species along the way. The chemical reaction rates can vary significantly depending on the conditions of the system and the relative concentration of constituent species within the mixture. In particular, the reaction rate has a highly non–linear dependence on the local temperature which introduces a range of different chemical timescales. In practise, the global reaction of a gas mixture features hundreds, if not thousands, of elementary steps throughout the entire process. Each step involves the creation and destruction of a vast array of different intermediate chemical species. It is impractical to account for all of these interactions, so it is important to determine which elementary steps are significant to the analysis in terms of the species that are involved and the energy that is released. Thankfully most of the energy released by the global reaction can often be attributed to a comparatively small number of key elementary reactions. The challenge lies in identifying which intermediate steps are to be included in the mechanism that governs the chemical kinetics of the model.

The other primary factor influencing the combustion process is the flow regime of the gas mixture. The convective nature of the flow has a dominant effect on combustion and influences almost every aspect of the system. The motion of a fluid is described by the Navier–Stokes (NS) equations, which give an accurate representation of fluid behaviour across a wide range of flow conditions. The full set of NS equations have developed a reputation for being notoriously difficult to solve and there are no closed form, analytic solutions known to exist. Despite this, we can obtain numerical solutions to the discretised NS equations and they have proven to be remarkably useful for engineering purposes. Almost all combustion processes relevant to an engineering context occur under a turbulent flow regime. Turbulence holds an interesting place in the history of modern science and documented studies of the topic date back to the Renaissance period. Figure 1.1 features an impressive sketch by Leonardo da Vinci that captures the innate swirling motions that are associated with turbulent flow. Many of the difficulties associated with the NS equations are attributed to turbulent phenomena [34] and a fundamental theory of turbulence is yet to be established. There is not even a concise or universally accepted definition of what turbulence actually is. According to Bradshaw [35], “the only short but satisfactory answer to the question “What is turbulence?” is that it is the general solution of the Navier–Stokes equations”. Nevertheless, much is still known about turbulence from a phenomenological perspective and it can be clearly identified by a number of defining characteristics. As opposed to the smooth and regular motion attributed to laminar flow, turbulent flow is distinguished by a velocity field that features highly chaotic and seemingly random fluctuations. The irregular motions do exhibit a certain degree of order in that they tend to manifest as swirling structures called eddies that occur throughout the flow field across scales ranging from the size of the entire fluid body, all the way down to the molecular level.

Figure 1.1: *An early illustration of turbulent eddies by Leonardo da Vinci [36].*

Constructing a model that includes both combustion and turbulence is a complex task. The resulting system contains a ludicrous number of degrees of freedom, and the interactions that occur throughout the domain are all coupled together. To get a full description of the flow using computational fluid dynamics (CFD), we use the NS equations for a multi–species reacting gas [37]. These are an extension of the conventional NS equations for compressible flows. With this formulation we can account for the changing thermal, chemical and transport properties of the flow, which can vary significantly with temperature and composition.

1.4 Objectives and Methodology

This study investigates the turbulent combustion processes that are highly relevant to aerospace propulsion. The purpose is to explore numerical techniques for switching between different types of fuel in a simulated combustion chamber that is based on the AFRL test rig [38]. A virtual representation of the AFRL test rig is used to model the premixed turbulent combustion of different fuel types. The simulations are intended to reproduce the same system conditions and combustion dynamics that are observed in the physical test case.

To simulate the combustion process, a *reaction mechanism* is incorporated into the CFD model. The reaction mechanism describes the chemical transformations and energy exchange that occur when a fuel and an oxidiser react. It includes information related to the chemistry, thermodynamics and molecular transport of the individual chemical species that make up the reacting gas mixture. Different reaction mechanisms describe different possible paths for the chemical process to take a reactant and convert it to a product. Full chemical mechanisms contain a broad set of instructions that incorporate enough chemistry for a highly detailed analysis of a wide range of different fuel types. They can feature hundreds of intermediate steps involving the creation and destruction of dozens of intermediate chemical species. A comprehensive reaction mechanism like this is superfluous and extremely computationally expensive. The most important chemical processes for combusting a certain fuel can often be reduced to a far smaller number of steps that account for the vast majority of the mass and energy transformations. These are known as skeletal reaction mechanisms. At the other end of the spectrum we find global reaction mechanisms that use a single step to convert the reactants into products with no intermediate processes. They can deliver useful results at a much lower computational cost, but can also miss out on important features such as flame quenching and ignition delay. The decision to use a certain reaction mechanism is an important aspect of combustion modelling. Fuel–specific mechanisms are used for each type of fuel that is modelled.

Large eddy simulation (LES) techniques are used to solve the governing equations. This ensures that the largest turbulent structures are captured in the solution and are well resolved. Flow phenomena that occurs on scales smaller than the size of a computational grid cell is modelled. A one–equation dynamic kinetic energy subgrid model [39] is used to account for small–scale turbulent fluctuations that are not resolved at grid level. This turbulence model dynamically updates the model coefficients and computes the subgrid stresses based on the local flow conditions. A subgrid model is also needed for small–scale chemical activity. Important steps of the reaction process take place within the leading *front* of the flame body which is much smaller than the size of a computational cell. The thickened flame model [40] is used to artificially thicken the flame so that it can be resolved at grid level.

First, a premixed propane–air combustion model is built according to the test case specifications given by the Model Validation for Propulsion (MVP) Workshop [41]. In this thesis we use the recommended reaction mechanisms for the MVP test case; the semiglobal Ghani mechanism [42]. Experimental data for the MVP test case is provided by Fugger et al. [43], who measured the propane flame characteristics in the AFRL combustor. Fureby [44] investigated the MVP case using the Z66 mechanism with a dynamic kinetic energy subgrid turbulence model, and a partially–stirred reactor model for the subgrid chemistry. These studies are used for comparing and validating the propane combustion model developed for this thesis.

Once a dependable CFD model for propane combustion has been built, the fuel is switched from propane to hydrogen. The hydrogen model uses the Z22 reaction mechanism given by Zettervall and Fureby [45], which was developed specifically for hydrogen combustion. This mechanism has been shown to give good agreement with test data obtained from supersonic ramjet combustor experiments [46]. It has also been demonstrated that Z22 is capable of correctly predicting the combustion dynamics of a hydrogen–air flame in LES combustion models [47].

Because hydrogen and propane have vastly different physical properties, switching the fuel alters the combustion dynamics of the entire system. Unlike the propane case, there are no set up specifications or specific guidelines available for constructing the hydrogen model. The objective is therefore to determine how to configure the model such that particular qualities and quantities of the hydrogen combustion process match up with the corresponding qualities and quantities for the combustion of propane. System variables, such as the fuel concentration and the inlet velocity, are adjusted so that certain properties of the hydrogen model are equivalent to that of the propane model. By adapting hydrogen to the validated model for propane, we gain confidence that the combustion system is representative of a physical test case for hydrogen combustion. While this is no substitute for empirical data, we nevertheless gain insight into the turbulent combustion dynamics of hydrogen fuel.

2 Theory

2.1 General Forms

2.1.1 Primitive Variables

A uniform gas mixture is assumed to contain fixed proportions of its constituent chemical species for any given region within the system. When the chemical composition of the gas is transformed through combustion, the relative amounts of each of the reacting species will change and new species will be either created or destroyed in the process. To track the change in mixture composition we introduce the species mass fraction, Y_k. Poinsot and Veynante [37] define the mass fraction as

$$Y_k = \frac{m_k}{m} \tag{2.1}$$

$$\sum_{k=1}^{N} Y_k = 1 \tag{2.2}$$

Here, m_k is the mass of species k contained within a fixed control volume (CV), m is the total mass of the gas mixture within the CV and N is the number of species present within the system. By definition, the sum of the species mass fractions must always equal one. Let us denote the total density of the ideal gas mixture inside the CV as ρ. The partial density for any given species, ρ_k, is then defined as the product of the total density and the k^{th} mass fraction [37]. It follows that the sum of all N partial densities must equal the total density of the ideal gas mixture contained in the CV.

$$\rho_k = \rho Y_k \tag{2.3}$$

$$\rho = \sum_{k=1}^{N} \rho_k \tag{2.4}$$

The partial pressure of any particular species, p_k, is obtained with ρ_k via the ideal gas law. Summing all N partial pressures gives the thermodynamic equation of state for an ideal gas mixture [48].

$$p_k = \rho_k \frac{R_u}{W_k} T \tag{2.5}$$

$$p = \sum_{k=1}^{N} p_k \tag{2.6}$$

$$p = \rho \frac{R_u}{W} T \tag{2.7}$$

Here, R_u is the universal gas constant, T is the gas temperature, W is the mean molecular weight of the mixture and W_k is the molecular weight of the k^{th} species. From Eqs. (2.3) to (2.7), it follows that the mean molecular weight of an ideal gas mixture is given by

$$\frac{1}{W} = \sum_{k=1}^{N} \frac{Y_k}{W_k} \tag{2.8}$$

For reacting flows it is sometimes convenient to calculate mixture composition in terms of the mole fraction and the molar concentration. The mole fraction, X_k, is the ratio of the number of moles of a given species, n_k, to the total number of moles, n, inside the CV. The molar concentration, $[X_k]$, is the number of moles per unit volume of the species k. The following definitions are given according to Poinsot and Veynante [37].

$$X_k = \frac{n_k}{n} \tag{2.9}$$

$$X_k = \frac{W}{W_k} Y_k \tag{2.10}$$

$$[X_k] = \rho \frac{Y_k}{W_k} \tag{2.11}$$

The primitive variables and all forthcoming quantities of significance are listed in the nomenclature with their corresponding SI units.

2.1.2 Thermodynamics

At any given position within a reacting flow, the total energy, E, comes in the form of either internal energy or kinetic energy. It can be expressed in a variety of forms depending on the particular case at hand [37]. Here we define the total, non–chemical, energy as

$$E = h_s - \frac{p}{\rho} + \frac{u_i u_i}{2} \tag{2.12}$$

Here, h_s is the sensible enthalpy of the flow. The second term in Eq. (2.12) represents the transfer of energy through expansion and the third term is the kinetic energy of the bulk flow. The value of h_s is calculated by obtaining the sum of all species contributions

$$h_s = \sum_{k=1}^{N} h_{s,k} Y_k \tag{2.13}$$

$$h_{s,k} = \int_{T_{\mathrm{ref}}}^{T} C_{p,k} \, \mathrm{d}T \tag{2.14}$$

Here, $h_{s,k}$ and $C_{p,k}$ is the sensible enthalpy and the heat capacity of the k^{th} species, respectively.

The physical characteristics of a multicomponent gas mixture are influenced by the properties of each chemical species, all of which have varying degrees of temperature dependence. Here we define quantities related to molecular transport that appear in the governing equations and depend on temperature and species composition. The theoretical basis for these equations come from statistical mechanics and kinetic theory [49]. They are presented in the form used by Fluent, as described in the user documentation [50].

The dynamic viscosity of the mixture is needed for the momentum equation and the energy equation. The total viscosity, μ, depends on the sum of the partial viscosities of each species, μ_k. It is calculated by

$$\mu = \sum_{k=1}^{N} \frac{X_k \mu_k}{\sum_{i=1}^{N} X_i \Phi_{ki}} \tag{2.15}$$

$$\mu_k = 2.67{\times}10^{-6} \left(\frac{(W_k T)^{1/2}}{\sigma_k^2 \, \Omega_k} \right) \tag{2.16}$$

$$\Phi_{ki} = \frac{\left(1 + \left(\frac{\mu_k}{\mu_i}\right)^{1/2} \left(\frac{W_k}{W_i}\right)^{1/4}\right)^{1/2}}{8\left(1 + \frac{W_k}{W_i}\right)^{1/2}} \tag{2.17}$$

$$\Omega_k = \Omega_k(T, \epsilon_k / k_B) \tag{2.18}$$

Here, σ_k and ϵ_k are the Lennard–Jones parameters for length and energy, respectively. Ω_k is the collision integral [51], and k_B is the Boltzmann constant.

The total thermal conductivity, λ, depends on the sum of partial thermal conductivities of each species, λ_k. It is needed for the energy equation and is calculated by

$$\lambda = \sum_{k=1}^{N} \frac{X_k \lambda_k}{\sum_{i=1}^{N} X_i \Phi_{ki}} \tag{2.19}$$

$$\lambda_k = \frac{15 R_u}{4W} \mu \left(\frac{4 C_p W}{15 R_u} + \frac{1}{3} \right) \tag{2.20}$$

Here, R_u is the universal gas constant and C_p is the total specific heat capacity of the gas mixture. The specific heat capacity is determined from the NASA–7 polynomial equations [52]

$$\frac{C_{p,k}}{R_u} = a_1 + a_2 T + a_3 T^2 + a4 T^3 + a_5 T^4 \tag{2.21}$$

$$C_p = \sum_{k=1}^{N} C_{p,k} Y_k \tag{2.22}$$

The coefficient values a_1 to a_5 are required to define $C_{p,k}$ for each chemical species. Additional values are used to specify the bounds or extend the range of the polynomial.

The diffusive properties of a particular chemical species must account for how it diffuses into different mixtures that contain different concentrations of other species. The mass diffusion coefficient, D_k, is needed for the energy and species transport equations. It is given by

$$D_k = -\frac{\sum\limits_{i\neq k} X_i}{\sum\limits_{i\neq k} (X_i/\mathcal{D}_{ik})} \tag{2.23}$$

$$\mathcal{D}_{ik} = 0.00188 \frac{\left(T^3\left(\frac{1}{W_i} + \frac{1}{W_k}\right)\right)^{1/2}}{p\, \sigma_k^2\, \Omega_k} \tag{2.24}$$

Here, $\mathcal{D}_{ik}$ is the binary mass diffusion coefficient for species i into species k. Thermal diffusion is neglected here.

2.2 Chemical Kinetics

2.2.1 Mixture Composition

The stoichiometric ratio of the oxidiser mass fraction, Y_O, to the fuel mass fraction, Y_F, is given by

$$s = \left(\frac{Y_O}{Y_F}\right)_{\mathrm{st}} \tag{2.25}$$

Complete global combustion of an unburnt gas mixture at stoichiometric conditions will consume all of the fuel and oxidiser species. The equivalence ratio, ϕ, is used to represent the concentration of fuel species relative to stoichiometric conditions. It is defined as the product of the stoichiometric ratio and the mass fraction ratio of fuel to oxidiser

$$\phi = s\frac{Y_F}{Y_O} \tag{2.26}$$

Unburnt mixtures with $\phi > 1$ are called *fuel–rich* and will consume all of the oxidiser content with unburnt fuel species left over. If $\phi < 1$ then the mixture is *fuel–lean.* Once all the fuel is spent the combustion will terminate and the final mixture will contain unburnt oxidiser species. Stoichiometric mixtures have an equivalence ratio equal to one. The equivalence ratio is a convenient way to quantify the fuel content in the context of premixed combustion.

2.2.2 Thermochemistry

Heat of Combustion

The heat released by the combustion process is introduced through the sensible enthalpy term and it is important to describe how this works. The total enthalpy of a particular chemical species, h_k, is equal to the sum of its sensible enthalpy and its standard enthalpy of formation

$$h_k = h_{s,k} + \Delta h^{\circ}_{f,k} \tag{2.27}$$

Here, the enthalpy of formation, $\Delta h^{\circ}_{f,k}$, is defined as the change in enthalpy required to produce 1 kg of a chemical species at the standard reference conditions of $p = 1$ atm and $T_{\mathrm{ref}} = 298.15$ K. By definition, the enthalpy of formation for both H_2 and O_2 at standard state conditions is $\Delta h^{\circ}_{f,k} = 0$ J. This is because both species are made up from a single type of element and are most stable in diatomic form. The combustion of the two compounds will see them combine to form water, as shown in the single step reaction equation

$$\mathrm{H_2} + \frac{1}{2}\,\mathrm{O_2} \longrightarrow \mathrm{H_2O} \tag{2.28}$$

For H_2O we have $\Delta h^{\circ}_{f,\mathrm{H_2O}} = -1.205{\times}10^{8}$ J/kg (for the vapor state of H_2O). This is a negative value because the energy required to break the chemical bonds in the H_2 and O_2 molecules is less than the energy required to reconfigure the bonds and bind the H_2O molecules together. The surplus energy has escaped in the form of heat. Combustion reactions are exothermic, so the combined formation enthalpies of the initial reactant species is smaller in magnitude than the combined formation enthalpies of the final product species.

The heat released by the reaction is directly related to the difference in standard state formation enthalpy between the reactant and product species. Assume that a constant pressure reaction takes place and all reactant species are transformed into product species, as heat is released in the process. Once the reaction is complete, the temperature of the burnt product mixture will be greater than the initial temperature of the unburnt reactant mixture. If the burnt gas were to be cooled down to the same initial temperature of the unburnt gas, we would find that the sum of species formation enthalpies of the product mixture is different to that of the reactant mixture. The change in formation enthalpies corresponds to the net heat that was generated by the reaction. This is known as the heat of combustion, Q. It is given as

$$Q = -\Delta_r h_f^\circ = -\left(\Delta h_{f,\mathrm{pr}}^\circ - \Delta h_{f,\mathrm{re}}^\circ\right) \tag{2.29}$$

Here, $\Delta h_{f,\mathrm{re}}^\circ$ and $\Delta h_{f,\mathrm{pr}}^\circ$ are the net formation enthalpies of the reactant and product mixtures, respectively. The heat of combustion plays a central role in this thesis. It is used as a point of reference to calibrate the system parameters.

A solution may be obtained immediately if all the species formation enthalpies and the unburnt mixture composition is known. A balanced chemical equation will reveal the corresponding burnt mixture composition. From the first law of thermodynamics we know that for a closed adiabatic system at constant pressure where no work is done, the total enthalpy of the mixture is conserved. Given that $\mathrm{d}h = 0$ and we ensure that all values are calculated for standard state reference conditions, we can rearrange Eq. (2.27) and sum the sensible enthalpies of all N species. Inserting this into Eq. (2.29) gives the heat of combustion for the reaction as

$$Q = \sum_{k=1}^{N} h_{s,k} Y_k \tag{2.30}$$

Note that this applies to an idealised case and is only valid under assumptions that do not hold in practice. Other factors, such as the fleeting existence of intermediate species, variable reaction rates and the influence of mechanical mixing must also be considered. We will discuss such matters as the theory is expanded throughout this section.

Thermodynamic Equilibrium

Given the energy content of a system, thermodynamic calculations can be used to predict whether a spontaneous combustion event is possible. A process is considered to be spontaneous if the total entropy of a closed system can increase as a consequence of the process occurring under a prescribed set of conditions [53]. Spontaneity is governed by the second law of thermodynamics and provides the inherent driving force towards chemical equilibrium. The chemical expression given in Eq. (2.28) is a forward reaction and represents a one–way process that simply converts reactants into products. This is only half of the story.

For every forward reaction there is a corresponding backward reaction. Once a particular product species has been created in an elementary reaction, certain conditions may permit it to participate in subsequent elementary reactions. In that case, the former product will assume the role of a reactant and continue to bond with other molecules as the global reaction process continues along the chemical pathway. Reversible reactions are also necessary if we are to include the effects of molecular disassociation. For a chemical system containing N chemical species that are reacting through M reactions, the stoichiometric balance equation has the form

$$\sum_{k=1}^{N} \nu'_{kj} \mathcal{M}_k \rightleftharpoons \sum_{k=1}^{N} \nu''_{kj} \mathcal{M}_k \tag{2.31}$$

Here, $\mathcal{M}_k$ denotes the k^{th} chemical species, ν'_{kj} and ν''_{kj} denote the stochiometric coefficients for the k^{th} chemical species in the j^{th} reaction, respectively. The two–way arrow in Eq. (2.31) indicates that it is a reversible reaction and can proceed in both directions. It follows that product and reactant species can *both* be created and destroyed throughout the reaction process. From the conservation of mass, we can state Eq. (2.31) in terms of W_k as

$$\sum_{k=1}^{N} \nu_{kj} W_k = 0 \tag{2.32}$$

Here, ν_{kj} is the net stochiometric coefficient for the j^{th} reaction. It is defined as

$$\nu_{kj} = \nu''_{kj} - \nu'_{kj} \tag{2.33}$$

Equilibrium conditions are associated with the chemical potential of the species involved in the reaction. The thermodynamic state of the system at equilibrium is characterised by the Gibbs free energy. Gibbs free energy is a thermodynamic potential that represents the minimal in equilibrium compared to its values in other states with the same temperature and pressure [54]. It can be thought of as the amount of energy available to do non–pressure–volume work. Gibbs free energy, G, is an extensive system property that is defined by

$$G \equiv H - TS \tag{2.34}$$

Here, both H and S are given as the extensive system quantities for total enthalpy and total entropy, respectively. Gibbs free energy and chemical composition are related by expressing Eq. (2.34) as a function of pressure, temperature and numbers of moles. These are the natural variables for Gibbs free energy. Note that pressure and temperature are both intensive system properties, and that the number of moles is an extensive property. Since G is a thermodynamic potential, all other thermodynamic properties are obtained when the equation is solved using its natural variables [55]. The total derivative of the Gibbs state function $G = G(p, T, n_k)$ is given as

$$\mathrm{d}G = \left(\frac{\partial G}{\partial p}\right)_{T,n_k} \mathrm{d}p + \left(\frac{\partial G}{\partial T}\right)_{p,n_k} \mathrm{d}T + \sum_{k=1}^{N} \left(\frac{\partial G}{\partial n_k}\right)_{p,T} \mathrm{d}n_k \tag{2.35}$$

Holding pressure and temperature constant will eliminate the first two terms since $\mathrm{d}p = \mathrm{d}T = 0$. The state function $G(p, T, n_k)$ is first order homogeneous in terms of the extensive property n_k, which means that the two quantities scale linearly. As a consequence, we can apply Euler‘s homogeneous function theorem [56] so that the equation becomes

$$G = \sum_{k=1}^{N} \upsilon_k n_k \tag{2.36}$$

$$\upsilon_k = \left(\frac{\partial G}{\partial n_k}\right)_{p,T} \tag{2.37}$$

The new variable, υ_k, represents the chemical potential of species k and is defined as the k^{th} partial molar derivative of G. Using Eq. (2.36), we can now state the general condition for chemical equilibrium as

$$\sum_{k=1}^{N} \upsilon_k n_k = 0 \tag{2.38}$$

Gibbs free energy must be related to the species composition of the reacting mixture so that it can influence the chemical pathway. A progress variable, ξ, is introduced to define the extent of reaction progress. The extent of reaction represents an infinitesimal change between the number of moles at the initial state and the number of moles at the final state. The change in number of moles of each species is normalised by its stoichiometric coefficient, such that

$$\mathrm{d}\xi = \frac{\mathrm{d}n_k}{\nu_k} \tag{2.39}$$

Here, ν_k is the stoichiometric coefficient given in Eq. (2.33). Notice that the value of ν_k is positive for products and negative for reactants. Ensuring that pressure and temperature remain constant, we combine Eqs. (2.35), (2.37) and (2.39) to express the change in Gibbs free energy as

$$\mathrm{d}G = \sum_{k=1}^{N} \upsilon_k \nu_k \mathrm{d}\xi \tag{2.40}$$

For a combustible system at constant pressure, the change in Gibbs free energy can be determined if the temperature and species composition is known. Then we can calculate the point chemical equilibrium that the system will spontaneously advance towards. From Eqs. (2.33), (2.39) and (2.40), we can deduce that the direction towards equilibrium is set by $\mathrm{d}\xi > 0$ for a forward reaction and $\mathrm{d}\xi < 0$ for a backward reaction. It follows that the curve describing Gibbs free energy has a minimum value which corresponds to the equilibrium state, as shown in Figure 2.1.

For any point along the curve, the reaction Gibbs energy, $\Delta_r G$, is defined as the slope of the tangent line at that point. It is formally expressed as

$$\Delta_r G \equiv \left(\frac{\partial G}{\partial \xi}\right)_{p,T} \tag{2.41}$$

The species composition of the equilibrium mixture at $\Delta_r G = 0$ has the lowest chemical potential of all other possible microstate combinations at the prescribed pressure and temperature. However, it is important to note that $\Delta_r G$ is not identical to $\mathrm{d}G$. The equilibrium state is given according to the initial state of the system. A transition between the two states involves a change that can affect the pre–determined conditions of the equilibrium state. In order to complete the full reaction path there must be some degree of mechanical mixing to allow the intermediate species to encounter each other and complete the full sequence of elementary reactions. The mixing results in an inescapable change in entropy because we are bound by the second law of thermodynamics where $dS > 0$ for an isolated system. As a consequence, any progression towards equilibrium will immediately alter the entropy of the system and shift the equilibrium position. This is because the conditions for the equilibrium state are set for explicit values of pressure, temperature and species composition. Any discernible change in reaction extent results in a new equilibrium state that is different from the first equilibrium state.

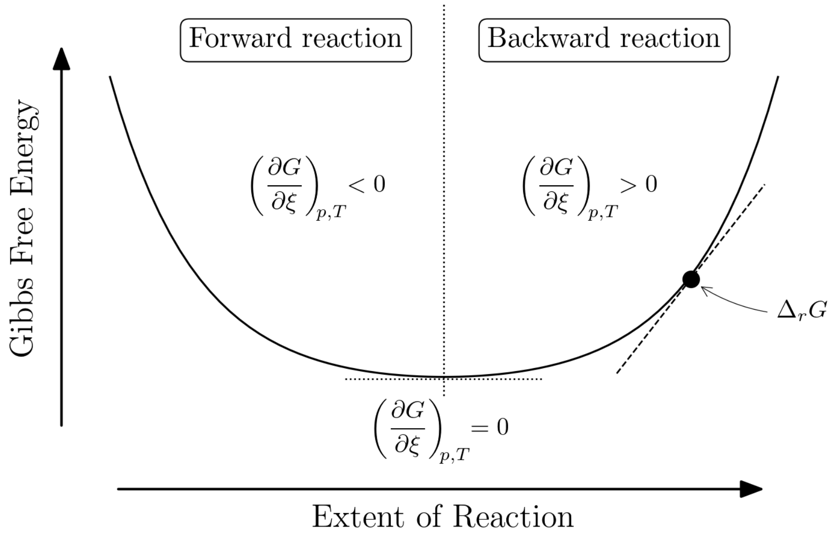

Figure 2.1: *Gibbs free energy at constant pressure and temperature. The reaction Gibbs energy at the point on the curve indicated by $\Delta_r G > 0$ corresponds to a mixture state with an excess of product species. At this prescribed p and T, a spontaneous thermodynamic process will favour the backward direction.*

Fortunately, this is of no concern because we are only seeking the *direction* that a spontaneous thermodynamic process must take, as per the second law of thermodynamics. Every possible state configuration will be pointed towards equilibrium by $\Delta_r G$, which is well defined for any configuration of p, T and n_k. The extent of reaction can oscillate about the equilibrium position indefinitely, but the thermodynamic limit always converges to $\Delta_r G \to 0$ as the system approaches maximum entropy. This corresponds to a system that is driven along a reaction pathway that minimises Gibbs free energy that is controlled by the arithmetic sign of $\mathrm{d}\xi$ so that all spontaneous chemical change proceeds in the correct direction. The difference in Gibbs free energy between an unburnt mixture of product species and a burnt mixture of reactant species, provides all of the information necessary to calculate important combustion variables. Important quantities, such as the heat of combustion, can be reliably estimated and used to develop the CFD models for the primary analysis.

The equilibrium method is independent of time and the chemistry is assumed to occur infinitely quickly. It is valid in many situations since chemical timescales are often orders of magnitude faster than mechanical timescales. Knowledge of a combustion system's unburnt and burnt states is valuable for configuring new models and verifying existing results. However, the above calculations are path independent and do not describe the transient processes that convert reactants into products. The timescales associated with turbulent combustion can be comparable to chemical timescales and have a considerable influence on the nature of the system. A combustion process that progresses in time may approach chemical equilibrium, but this does not suggest that combustion is on the verge of extinction. If the system is continuously replenished with unburnt reactants, the chemical equilibrium state indicates a balance in the *rate* of reaction between the forward and backward directions. In practice, all chemical transformation processes occur in finite time and the primary objective of chemical kinetics is to determine the reaction rate.

2.2.3 Finite Rate Chemistry

Law of Mass Action

In the context of combustion, an elementary reaction will occur once a molecule has absorbed enough energy to destabilise its molecular structure. Most new species are formed when unstable molecules exchange atoms during bimolecular or trimolecular collision events. Unimolecular reactions can also occur if an unstable molecule collides with an inert molecule, causing it to break apart and form new species by disassociation [33]. Some of these chemical processes can happen on timescales that are orders of magnitude greater than the others. Finite rate chemistry (FRC) is used to track the changes in species concentration and control the reaction rates as time advances. According to the law of mass action, the rate of reaction is proportional to the product of the concentrations of the reactant species, with each concentration being raised to a power equal to the corresponding stoichiometric coefficient [57]. Building on Eq. (2.33), we can express the net production rate of a given species, $\dot{\omega}_k$, for a series of M reversible reactions featuring a total of N chemical species as follows

$$\dot{\omega}_k = W_k \sum_{j=1}^{M} \nu_{kj} \mathcal{Q}_j \tag{2.42}$$

$$\mathcal{Q}_j = K_{F,j} \prod_{\ell=1}^{N} [X_\ell]^{\nu'_{\ell j}} - K_{B,j} \prod_{\ell=1}^{N} [X_\ell]^{\nu''_{\ell j}} \tag{2.43}$$

Here, $\mathcal{Q}_j$, is the reaction rate of the j^{th} reaction. The reaction rate constants associated with the forward and backward directions are denoted $K_{F,j}$ and $K_{B,j}$, respectively. Each species that participates in reaction j is represented by its molar concentration, $[X_\ell]$. Equation (2.42) will feature as a term in the governing equations. Therefore, $\dot{\omega}_k$ must be a known quantity before we can solve the species transport equation. It should also be noted that the reaction rate constants are, in fact, not constant, but highly non–linear functions of temperature.

To demonstrate how FRC is implemented, we consider the following two–step reaction process for the combustion of propane.

$$\mathrm{C_3H_8} + 3.5\,\mathrm{O_2} \longrightarrow 3\,\mathrm{CO} + 4\,\mathrm{H_2O} \tag{2.44}$$

$$\mathrm{CO} + 0.5\,\mathrm{O_2} \rightleftharpoons \mathrm{CO_2} \tag{2.45}$$

Note that Eq. (2.44) is a unidirectional reaction, while Eq. (2.45) is a reversible reaction that features a forward and backward component. The rate variable given in Eq. (2.43) is inserted into Eq. (2.42), letting $j = 1$ and $j = 2$, for the first and second reaction, respectively. By expanding the expression, we arrive at the equation for the net production rate of species k, according to the reaction path specified by Eqs. (2.44) and (2.45).

$$\dot{\omega}_k = W_k \Big(\nu_{k1} \big(K_{F,1} [\mathrm{C_3H_8}][\mathrm{O_2}]^{3.5} \big) + \nu_{k2} \big(K_{F,2} [\mathrm{CO}][\mathrm{O_2}]^{0.5} - K_{B,2} [\mathrm{CO_2}] \big) \Big) \tag{2.46}$$

$$\tag{2.47}$$

Here we have all N species and all M reactions contained in a single equation. The stoichiometric coefficient, ν_{kj}, ensures that the expression will reduce to the correct form, and only feature terms associated with the particular reactions that the k^{th} species participates in. For example, notice that carbon dioxide does not feature in the first reaction, given in Eq. (2.44). Therefore, if we let $k \to \mathrm{CO_2}$ then $\nu_{\mathrm{CO_2}1} = 0$ and $\nu_{\mathrm{CO_2}2} = -1$. In that case, all terms from reaction $j = 1$ disappear, and the net production rate of carbon dioxide becomes

$$\dot{\omega}_{\mathrm{CO_2}} = -W_{\mathrm{CO_2}} \big(K_{F,2} [\mathrm{CO}][\mathrm{O_2}]^{0.5} - K_{B,2} [\mathrm{CO_2}] \big) \tag{2.48}$$

Arrhenius Equation

The forward rate constant $K_{F,j}$ is typically modelled using the Arrhenius equation. If the reaction is reversible we also relate the forward and backward components through the equilibrium constant $K_{R,j}$. For every reaction j this gives

$$K_{F,j} = A_j T^{\beta_j} \exp\left(-\frac{E_{A,j}}{R_u T}\right) \tag{2.49}$$

$$K_{B,j} = \frac{K_{F,j}}{K_{R,j}} \tag{2.50}$$

$$K_{R,j} = \left(\frac{p_{\text{atm}}}{R_u T}\right)^{\sum_{\ell=1}^{N} \nu_{\ell j}} \exp\left(\frac{\Delta S_j^\circ}{R_u T} - \frac{\Delta H_j^\circ}{R_u T}\right) \tag{2.51}$$

Here, A_j is the pre–exponential constant, β_j is the temperature exponent, $E_{A,j}$ is the activation energy, ΔS_j° is the change in standard state entropy and ΔH_j° is the change in standard state enthalpy. Both standard state quantities in Eq. (2.51) are given in molar units. This is the approach that is used throughout this study. The production rate of each chemical species is calculated by substituting the Arrhenius equation into Eq. (2.43).

Also of importance to the chemical kinetics is the reaction activation energy, E_A. It represents the level of energy that is required to initiate a combustion reaction. If the temperature of an unburnt gas mixture is high enough, the occurrence probability of a collision event that is able to overcome the energy barrier goes from negligible to probable. Once the reaction begins more thermal energy is introduced to the system and combustion can be sustained as long as the reactants are continuously replenished.

Figure 2.2 shows how the energy profile of a combusting gas evolves. Initially, most of the energy is contained within the chemical bonds of the reactants, indicated by their large formation enthalpies. With enough thermal energy the activation energy will be achieved. The chemical bonds are then broken and the reactants begin to form products. Once the reaction has concluded, there is less potential left in the system since the chemical energy has been lost in the form of heat. The backward reaction can only take place if enough potential is regained such that the energy level remains near that of the activation energy.

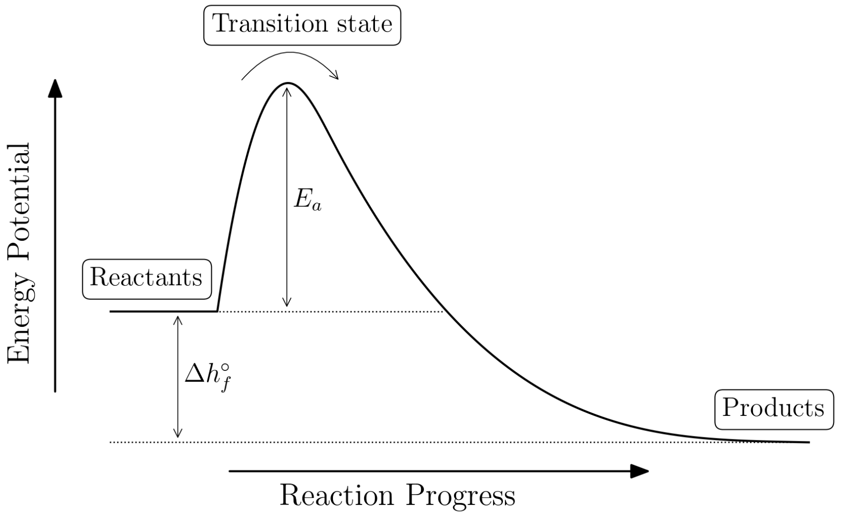

Figure 2.2: *Activation energy profile.*

2.3 Governing Equations

The conservation of mass and momentum is given by the NS equations for a compressible fluid with variable viscosity and heat conductivity. The transport equation for the conservation of energy is included. For multicomponent gas mixtures we introduce additional transport equations to account for the formation, motion and destruction of each chemical species involved in the combustion process.

2.3.1 Mass Conservation

Typically referred to as the continuity equation, the conservation of mass is given as

$$\frac{\partial \rho}{\partial t} + \frac{\partial}{\partial x_j}(\rho u_j) = 0 \tag{2.52}$$

Here, ρ is density, t is time, u_j is the j^{th} component of the velocity vector $\mathbf{u} = (u, v, w)$ and x_j is the j^{th} component of the position vector $\mathbf{x} = (x, y, z)$.

2.3.2 Momentum Conservation

The expression for conservation of momentum is essentially Newton's second law applied to a fluid continuum. It is given as

$$\frac{\partial}{\partial t}(\rho u_i) + \frac{\partial}{\partial x_j}(\rho u_i u_j) = -\frac{\partial p}{\partial x_i} + \frac{\partial \tau_{ij}}{\partial x_j} \tag{2.53}$$

The first and second term on the left–hand side (LHS) describe the transient and convective behaviour of the flow, respectively. Any forces acting on the fluid must be either internal or external in origin. The effects of external forces, including gravity, are considered negligible for the current study and are therefore not included. Internal forces are split up into those acting in the normal direction and those acting tangentially. Normal stresses are represented by the pressure term and shear stresses are represented by the viscous term. Viscous effects are described by the viscous stress tensor which has the form

$$\tau_{ij} = \mu\left(\frac{\partial u_i}{\partial x_j} + \frac{\partial u_j}{\partial x_i} - \frac{2}{3}\frac{\partial u_k}{\partial x_k}\delta_{ij}\right) \tag{2.54}$$

Here, the velocity gradients correspond to the rate of strain on the fluid. The stress tensor is a traceless quantity so the third term inside the brackets of Eq. (2.54) is necessary for the expression to remain valid upon tensor contraction.

2.3.3 Energy Conservation

The expression for the energy transport equation is given as

$$\frac{\partial}{\partial t}(\rho E) + \frac{\partial}{\partial x_j}(u_j(\rho E + p)) = \frac{\partial}{\partial x_j}\left(\lambda \frac{\partial T}{\partial x_j} - \rho \sum_{k=1}^{N} h_{s,k} D_k \frac{\partial Y_k}{\partial x_j} + \tau_{ij} u_i\right) \tag{2.55}$$

The first term in brackets on the right–hand side (RHS) represents the diffusion of thermal energy via conduction, where λ is given by Eq. (2.19). The second term in brackets on the RHS represents the diffusion of species with different enthalpies, where Y_k, $h_{s,k}$ and D_k are given by Eqs. (2.1), (2.14) and (2.23), respectively. The third term in brackets on the RHS acts as a source term which accounts for the energy generated by viscous work where τ_{ij} is given by Eq. (2.54).

2.3.4 Species Conservation

The conservation equation for Y_k is given for the transport of each chemical species k, in the form

$$\frac{\partial}{\partial t}(\rho Y_k) + \frac{\partial}{\partial x_j}(\rho u_j Y_k) = \frac{\partial}{\partial x_j}\left(\rho D_k \frac{\partial Y_k}{\partial x_j}\right) + \dot{\omega}_k \tag{2.56}$$

Here, D_k is the mass diffusion coefficient given in Eq. (2.23) and $\dot{\omega}_k$ is the reaction rate given in Eq. (2.42). Recall that Eq. (2.2) states that the sum of all N species mass fractions must equal one. We therefore have to satisfy an addition expression for Y_k. Since there is now a total of $N + 1$ equations for Y_k yet there are only N unknown values of Y_k, we are left with an overdetermined system that is mathematically inconsistent. To avoid this, Eq. (2.56) is only solved for $N-1$ species, and the remaining species mass fraction, Y_N, is obtained by

$$Y_N = 1 - \sum_{k=1}^{N-1} Y_k \tag{2.57}$$

Here, Y_N often represents the mass fraction of a diluent substance, such as N_2 gas in air [37].

2.4 Turbulent Flow

2.4.1 Turbulence Fundamentals

According to Poinsot and Veynante [37] "The main effect of turbulence on combustion is to increase the combustion rate". This is because of its ability to transport and mix fluid much more effectively than a comparable laminar flow [58]. A laminar flow is more than adequate for simply delivering unburnt reactant species to the flame front, but there is very little else it can do to assist combustion. Laminar flows typically travel along steady, uniform steam lines and feature very little lateral motion. The primary means of mixing is by mass diffusion which is usually a slow process compared to the fast–acting chemical reactions. Most combustion applications require that the flow is turbulent because its superior mixing qualities act rapidly across a much wider range of scales.

The nature of the flow regime can be identified by the Reynolds number. The Reynolds number, Re, relates the inertial forces to the viscous forces that are acting on a fluid body and is defined as

$$Re = \frac{\rho \mathcal{U} \mathcal{L}}{\mu} \tag{2.58}$$

Here, μ is the dynamic viscosity of the fluid, $\mathcal{U}$ is a velocity scale and $\mathcal{L}$ is a length scale, where the latter two are usually taken as the characteristic scales of the free–stream bulk flow. The Reynolds number is generally small for laminar flows and large for turbulent flows, but the transition between laminar and turbulent will vary depending on the geometry of the system. For flow through a round pipe the transition occurs at approximately $Re = 3000$ [58]. Notice that the variables on the RHS of Eq. (2.58) represent different aspects of the system. $\mathcal{L}$ is a property of the geometry, ρ and $\mathcal{U}$ are properties of the flow and μ is a property of the actual fluid.

Viscosity is a quantity of particular significance to fluid mechanics, and especially to turbulence modelling. It varies according to the temperature of the flow, so it must also be treated with care in the context of combustion. Analogous to the concept of friction for solid bodies, it is responsible for the dissipation of kinetic energy through irreversible heating. The influence of viscosity is represented by the shear stresses acting on a fluid element as it resists deformation under external loading.

The viscous stress tensor given in Eq. (2.54) governs how the kinetic energy of the flow is dissipated as heat. Most of the total kinetic energy is produced on the large scales of the flow where viscous dissipation typically is negligible. Dissipation only becomes dominant on the smallest scales. For this to happen, the kinetic energy is first transferred across the entire range of flow scales in what is called the cascade process. This describes how turbulent kinetic energy is passed down the energy spectrum via the interactions between similarly sized *eddies*, as shown in Figure 2.3.

An eddy can be thought of as a temporary vortex–like structure that have a characteristic length scale that is proportional to its diameter. The largest energy containing eddies are denoted with the length, velocity and time scales, ℓ_0, u_0, and t_0, respectively. The size of the largest eddies is generally on the order of the characteristic length associated with the bulk flow. At the other end of the spectrum we have the smallest turbulent scales, known as the Kolmogorov scales. The length, velocity and time scales associated with the smallest Kolmogorov eddies are denoted ℓ_η, u_η and t_η, respectively.

Consider the large eddy in the upper right corner of Figure 2.3, with the length scale ℓ_0. Now suppose that a fluid element is orbiting around the outer perimeter of that eddy and is travelling at the characteristic velocity u_0. The fluid element will complete a full orbital cycle in a time equal to the characteristic timescale of that eddy, t_0. Eddies are the links in the chain that descends down the energy spectrum. The cascade process reveals how kinetic energy is introduced, transferred and dissipated across the range of scales within the flow. Energy is given as a function of the wavenumber, $\kappa = 2\pi/\ell$. Note that the wavenumber is inversely propositional to the length scale. Large–scale eddies correspond to small wavenumbers and vice–versa for Kolmogorov scale eddies.

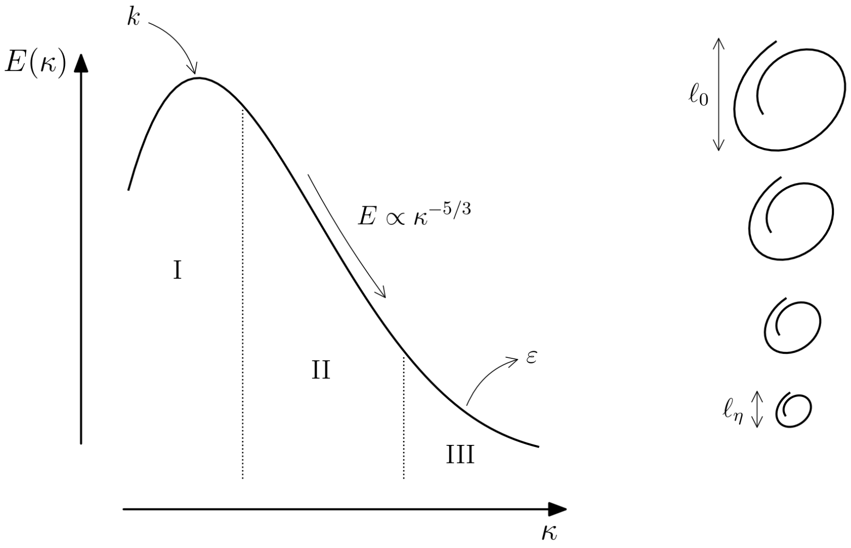

Figure 2.3: *Turbulent energy spectrum in terms of the wavenumber.*

To better illustrate cascade process we will follow the path down the energy spectrum by starting with a large energy containing eddy of length scale ℓ_0. It will have acquired its kinetic energy directly from the free–stream bulk flow and proceeded to go about its whirling motions. After a unit of time equal to t_0, we find that there has been a slight decrease in the characteristic length of that eddy. It has lost a small fraction of the energy it had just a moment ago. Of this, a very tiny part has been dissipated as heat due to viscous effects. But most of the energy loss is a result of brief interactions it shared with other eddies in the immediate vicinity. Within the duration of t_0 a small amount of kinetic energy was transferred from the large eddy to its smaller, yet comparable neighbours. As the eddies drift along the process repeats and they continue to feed on the energy of the bulk flow, while simultaneously being stripped of energy by slightly smaller eddies nearby. These events have all transpired on the largest scales of the flow, indicated as region I of the energy spectrum in Figure 2.3. The large–scale region features the largest eddies and therefore contains most of the total kinetic energy in the flow. The same events transpire as we move down the energy spectrum and through the inertial subregion, shown in Figure 2.3 as region II. The process of energy transfer is the same here as it is in region I, however these eddies behave independently of both the large–scale and Kolmogorov scale eddies. The inertial subregion is characterised by Kolmogorov's hypotheses [59], which state that the decay rate of the energy spectra in wavenumber space corresponds to the $-5/3$ power law. As the name suggests, this region is still heavily dominated by inertial effects and the effects of viscosity remain small. Only the very smallest eddies in region II are comparable to the largest eddies of the Kolmogorov scale so they can interact and continue to transfer energy. Eddies that are of the Kolmogorov scale exist in region III of Figure 2.3. In this region, the influence of inertia is finally overcome by viscous forces. Any remaining turbulent kinetic energy is dampened out and irreversibly converted into thermal energy.

Analytically, we can determine the total kinetic energy content of all eddies in the flow by integrating over the range of eddy sizes in wavenumber space

$$k = \int_0^\infty E(\kappa)\,\mathrm{d}\kappa \tag{2.59}$$

Here, k is the total kinetic energy and E is the kinetic energy per unit wavenumber for an eddy of wavenumber κ. The spectrum function $E(\kappa)$ represents the curve seen in Figure 2.3. Understanding the energy spectrum is essential to constructing reliable models of fluid flow. Because resolving the Kolmogorov scales is not feasible due to the high computational cost it requires, we must have a means of predicting the course of events that take place at the subgrid level. Combustion reactions also occur on scales below grid resolution and the processes feature strong coupling between turbulence and chemistry. Robust modelling techniques are needed so that we can have confidence that the system is behaving as expected at the subgrid level. These will be introduced in Section 2.4.3.

2.4.2 Large Eddy Simulations

The purpose of the LES method is to introduce scale separation by filtering the equations. The filtered equations are computed explicitly in order to fully resolve large–scale structures which contain most of the kinetic energy within the flow. To satisfy closure of the equations and account for information lost through the filter, all unresolved quantities must be modelled. Scale separation is achieved by the filtering of an arbitrary flow variable f

$$f = \overline{f} + f' \tag{2.60}$$

$$\overline{f}(\mathbf{x}) = \int f(\mathbf{x}')F(\mathbf{x}-\mathbf{x}')\,\mathrm{d}\mathbf{x}' \tag{2.61}$$

Here, $\overline{f}$ is the filtered quantity and f' is a perturbation with respect to the filtered quantity. The filter function, $F(\mathbf{x})$, is taken to be a box filter with compact support on a CV which is bounded by the computational grid cell used in the finite volume method. For compressible flow where density fluctuations are significant, the Favre filtering procedure is commonly employed. This serves to avoid creating additional unknowns that would otherwise arise from the decomposition of non–linear terms. The Favre filter is defined as

$$f = \widetilde{f} + f'' \tag{2.62}$$

$$\overline{\rho}\widetilde{f}(\mathbf{x}) = \int \rho f(\mathbf{x}')F(\mathbf{x}-\mathbf{x}')\,\mathrm{d}\mathbf{x}' \tag{2.63}$$

Here, $\widetilde{f}$ is the Favre filtered quantity and f'' is the corresponding perturbation. In practice, LES filtering is performed implicitly by the discretisation scheme. Scale separation is achieved at the cut–off between grid level and subgrid level. This corresponds to the size of a computational cell, denoted by Δ.

Figure 2.4 illustrates the effect that the filter has on the flow. This plot can be thought of as a time series of velocity in a fully developed turbulent flow field where the data has been measured with a test probe at a fixed position. The probe data shows that the local value of u oscillates at a wide range of seemingly random frequencies. The oscillations in the signal are caused by turbulent eddies that continuously pass over the probe. The frequency of oscillation is the time domain equivalent of the wavenumber so it is inversely propositional to the size of the eddy. By applying the filter, we preserve all of the large–scale energy containing eddies. Turbulent fluctuations that occur at scales smaller than the filter width Δ are removed from the signal.

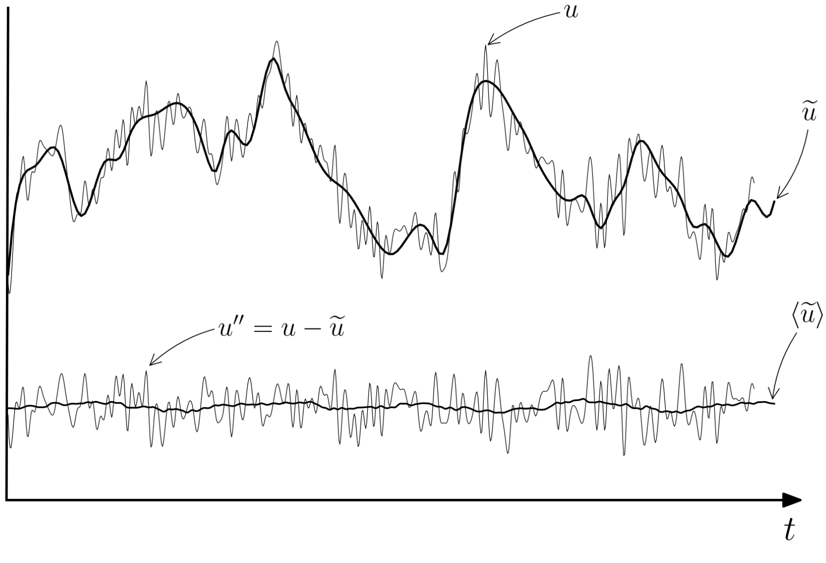

Figure 2.4: *Favre filtering and time averaging.*

In LES the computational mesh may be thought of as a kind of *virtual net* that captures all but the smallest of eddies. Using Eq. (2.62) we decompose the free stream velocity into the filtered component, $\widetilde{u}$, and the subgrid scale (SGS) fluctuating component, u''. We can see from Figure 2.4 that $\widetilde{u}$ still exhibits irregular behaviour and broadly resembles the bulk flow. Time series data is also used for post processing and it is useful to calculate the time–averaged velocity, $\langle\widetilde{u}\rangle$. In Figure 2.4 we can see that the filtered component is reduced to a near constant, while the SGS fluctuations have also been dampened, but still appear as perturbations about the mean velocity.

Here we review the mathematical procedure used to transform the governing equations into the filtered equations. The same process applied to all of the transport equations, so for this example we will use the momentum equation given in Eq. (2.53). It is more manageable to apply the filter to each term in the equation separately, instead of filtering the entire expression in a single operation. This is valid because the filter operator is a convolution product which is a linear transformation. First we consider the viscous term on the RHS of Eq. (2.53). Since it does not explicitly contain density, it is not regarded as a mass weighted quantity so the standard filter is used. Substituting this into Eq. (2.61) gives

$$\overline{\frac{\partial\tau_{ij}}{\partial x_i}}(\mathbf{x}) = \int \frac{\partial\tau_{ij}}{\partial x_i}(\mathbf{x}')\,F(\mathbf{x}-\mathbf{x}')\,\mathrm{d}\mathbf{x}' \tag{2.64}$$

$$= \frac{1}{\Delta^3}\iiint\limits_{\Delta} \frac{\partial\tau_{ij}}{\partial x_i}\,\mathrm{d}x'\,\mathrm{d}y'\,\mathrm{d}z' \tag{2.65}$$

Now we isolate τ_{ij} from the spatial derivative because we only want to integrate the filtered stresses, not the filtered *gradient* of the stresses. Strictly speaking, the filter operator and the spatial derivative operator do not commute when $\Delta = \Delta(x', y', z')$. However, the error introduced by interchanging integration and differentiation is of the same order as the finite volume discretization error, and is therefore acceptable. Therefore, we are free to proceed and move the differential outside of the integral.

$$\overline{\frac{\partial\tau_{ij}}{\partial x_i}} = \frac{\partial}{\partial x_i}\Big(\frac{1}{\Delta^3}\iiint\limits_{\Delta}\tau_{ij}\,\mathrm{d}x'\,\mathrm{d}y'\,\mathrm{d}z'\Big) \tag{2.66}$$

Now we can evaluate the integral over the CV and arrive at the final form of the gradient of the *filtered* viscous stress tensor, $\overline{\tau}_{ij}$.

$$\overline{\frac{\partial\tau_{ij}}{\partial x_i}} = \frac{\partial\overline{\tau}_{ij}}{\partial x_i} \tag{2.67}$$

Most terms that make up the filtered governing equations can be obtained in this way. If the quantity is mass–weighted then the Favre filter in Eq. (2.63) should be used instead. We can see that the same filtering procedure still applies if we recall that $\overline{\rho f} = \overline{\rho}\widetilde{f}$. The treatment of any non–linear terms is slightly different and they require extra attention. Here we consider the convective term in Eq. (2.53) which features a product between the velocities u_i and u_j. Since this term is mass–weighted we use the Favre filter and follow the steps given above to arrive at

$$\overline{\frac{\partial}{\partial x_i}(\rho u_i u_j)} = \frac{\partial}{\partial x_i}(\overline{\rho u_i u_j}) = \frac{\partial}{\partial x_i}(\overline{\rho}\,\widetilde{u_i u_j}) \tag{2.68}$$

Before addressing the non–linear elephant in the room we will filter the remaining terms Eq. (2.53) and put the expression back together.

$$\frac{\partial}{\partial t}(\overline{\rho}\widetilde{u}_i) + \frac{\partial}{\partial x_j}(\overline{\rho}\widetilde{u_i u_j}) = -\frac{\partial\overline{p}}{\partial x_i} + \frac{\partial\overline{\tau}_{ij}}{\partial x_j} \tag{2.69}$$

This is where the equations fight back. Because u_i and u_j are both filtered together we have fundamentally changed the nature of the convective term. To complicate matters further, $\widetilde{u_i u_j}$ is an unknown quantity so we now require an additional equation before a solution can be obtained. Note that the momentum equation only governs the transport of u_i. It does not transport the product $u_i u_j$. Likewise, the filtered momentum equation transports $\widetilde{u}_i$ and not $\widetilde{u_i u_j}$. Recall from Eq. (2.62) that the Favre filter separates the SGS velocity fluctuations from the rest of the flow field. Each of the unfiltered velocities, u_i and u_j, contain information about their own respective velocity fluctuations, u_i'' and u_j''. Since the act of filtering is numerically equivalent to calculating the average value for the CV, it follows that the non–linear correlation between u_i and u_i'' is immediately lost when we take the averaged product of u_i and u_j. The same goes for the correlation between

u_j and u''_j. Simply put, the product of the averaged velocities is not equal to the averaged product of the velocities [58]. The convective term in Eq. (2.69) can be written differently by adding and subtracting $\widetilde{u}_i\widetilde{u}_j$ to $\widetilde{u_i u_j}$ such that

$$\bar{\rho}\widetilde{u_i u_j} = \bar{\rho}\widetilde{u}_i\widetilde{u}_j + \bar{\rho}(\widetilde{u_i u_j} - \widetilde{u}_i\widetilde{u}_j) \tag{2.70}$$

This is inserted into Eq. (2.69), where the partial derivative of the bracketed term, $\bar{\rho}(\widetilde{u_i u_j} - \widetilde{u}_i\widetilde{u}_j)$, is separated from that of $\bar{\rho}\widetilde{u}_i\widetilde{u}_j$ and moved to the RHS of the equation. The convection term now contains the correct quantity for the transport of $\widetilde{u}_i$. The final form of the filtered momentum equation becomes

$$\frac{\partial}{\partial t}(\bar{\rho}\widetilde{u}_i) + \frac{\partial}{\partial x_j}(\bar{\rho}\widetilde{u}_i\widetilde{u}_j) = -\frac{\partial \bar{p}}{\partial x_i} + \frac{\partial}{\partial x_j}(\bar{\tau}_{ij} - \bar{\rho}(\widetilde{u_i u_j} - \widetilde{u}_i\widetilde{u}_j)) \tag{2.71}$$

Note that the bracketed term from Eq. (2.70) has been grouped with the viscous term. The expression $\bar{\rho}(\widetilde{u_i u_j} - \widetilde{u}_i\widetilde{u}_j)$ represents the unresolved Reynolds stresses.

All of the governing equations are filtered using the same approach, but there are some quantities that are treated differently. The filtered diffusion fluxes are modelled using the gradient assumption [37]. The SGS viscous dissipation is negligible [60] and not included in the filtered energy equation. The following unclosed terms appear in the filtered equations and require subgrid modelling:

- Unresolved Reynolds stress, $\bar{\rho}(\widetilde{u_i u_j} - \widetilde{u}_i\widetilde{u}_j)$
- Unresolved enthalpy flux, $\bar{\rho}(\widetilde{u_j h_s} - \widetilde{u}_j\widetilde{h}_s)$
- Unresolved species flux, $\bar{\rho}(\widetilde{u_j Y_k} - \widetilde{u}_j\widetilde{Y}_k)$

The full set of filtered equations for the transport of mass, momentum, energy and species are given as

$$\frac{\partial \bar{\rho}}{\partial t} + \frac{\partial}{\partial x_j}(\bar{\rho}\widetilde{u}_j) = 0 \tag{2.72}$$

$$\frac{\partial}{\partial t}(\bar{\rho}\widetilde{u}_i) + \frac{\partial}{\partial x_j}(\bar{\rho}\widetilde{u}_i\widetilde{u}_j) = -\frac{\partial \bar{p}}{\partial x_i} + \frac{\partial}{\partial x_j}(\bar{\tau}_{ij} - \bar{\rho}(\widetilde{u_i u_j} - \widetilde{u}_i\widetilde{u}_j)) \tag{2.73}$$

$$\frac{\partial}{\partial t}(\bar{\rho}\widetilde{E}) + \frac{\partial}{\partial x_j}\Big(\widetilde{u}_j(\bar{\rho}\widetilde{E} + \bar{p})\Big) = \frac{\partial}{\partial x_j}\left(\bar{\lambda}\frac{\partial \widetilde{T}}{\partial x_j} - \bar{\rho}\sum_{k=1}^{N}\widetilde{h}_{s,k}\bar{D}_k\frac{\partial \widetilde{Y}_k}{\partial x_j} + \bar{\tau}_{ij}\widetilde{u}_i - \bar{\rho}(\widetilde{u_j h_s} - \widetilde{u}_j\widetilde{h}_s)\right) \tag{2.74}$$

$$\frac{\partial}{\partial t}(\bar{\rho}\widetilde{Y}_k) + \frac{\partial}{\partial x_j}(\bar{\rho}\widetilde{u}_j\widetilde{Y}_k) = \frac{\partial}{\partial x_j}\left(\bar{\rho}\bar{D}_k\frac{\partial \widetilde{Y}_k}{\partial x_j} - \bar{\rho}(\widetilde{u_j Y_k} - \widetilde{u}_j\widetilde{Y}_k)\right) + \bar{\dot{\omega}}_k \tag{2.75}$$

2.4.3 Subgrid Modelling

Many important processes in a combustion system occur on very small scales. For non–reacting flows, the number of grid points required to fully resolve such processes can be estimated with the turbulent Reynolds number via a power law relationship [61]. It can become prohibitively expensive to fully resolve such processes for modest Reynolds numbers, let alone highly turbulent flows. The alternative is to use larger grid cells and adopt certain modelling techniques to account for the information that is lost through the grid filter.

Dynamic Subgrid Scale Kinetic Energy Model

The dynamic kinetic energy subgrid scale model [39] is used to determine the SGS Reynolds stresses and close Eq. (2.73). The SGS viscosity is computed in the process, and is used to model the unresolved flux terms so that we can also close Eqs. (2.74) and (2.75). LES models resolve the entire flow field above grid level and we can use some of this information to infer what is happening below grid level. Recall that kinetic energy is passed down the energy spectrum from large scales to small scales as described in Section 2.4.1. Here we use the transport equation for SGS turbulent kinetic energy to demonstrate how we quantify the amount of kinetic energy per unit time that is taken from the large scales and passed down to the small scales. This is known as the production and dissipation of turbulent kinetic energy and it takes place across all scales of the flow.

For now, we are specifically interested in length scales on the order of the computational grid scale, which lies within the inertial subregion shown in Figure 2.3. Because the kinetic energy that is dissipated on one scale is related to the kinetic energy that is produced on the next scale down, we can estimate the amount of SGS kinetic energy that is produced since it corresponds to the kinetic energy that is dissipated at grid level.

The SGS turbulent kinetic energy is given as

$$k_{sgs} = \frac{1}{2}(\widetilde{u_i u_i} - \widetilde{u}_i \widetilde{u}_i) \tag{2.76}$$

To understand how k_{sgs} is dissipated, we first need a value for the turbulent viscosity. Using dimensional analysis we can relate the SGS turbulent viscosity to the product of a velocity scale and a length scale.

$$\nu_t \sim \mathcal{U}\mathcal{L} \tag{2.77}$$

Velocity scales with the square root of kinetic energy, $\mathcal{U} \sim k_{sgs}^{1/2}$, and the length scale corresponds to the size of the grid filter, $\mathcal{L} \sim \overline{\Delta}$. Therefore, we can introduce a constant, C_k, to obtain a relationship for the turbulent viscosity. Since we are dealing with mass weighted quantities, we also include the density. Now we rewrite Eq. (2.77) as

$$\mu_t = \bar{\rho} C_k k_{sgs}^{1/2} \overline{\Delta} \tag{2.78}$$

Here, μ_t is the SGS turbulent viscosity. Assuming that the SGS Reynolds stresses from Eq. (2.73) take a similar form to that of the viscous stress tensor, τ_{ij}, in Eq. (2.54), we will let τ_{ij}^{sgs} represent the SGS stress tensor. After separating the isotropic and deviatoric components of τ_{ij}^{sgs} we can equate the unresolved Reynolds stresses to the SGS turbulent viscosity as follows

$$\tau_{ij}^{sgs} \equiv \bar{\rho}(\widetilde{u_i u_j} - \widetilde{u}_i \widetilde{u}_j) \tag{2.79}$$

$$\tau_{ij}^{sgs} - \frac{1}{3}\tau_{kk}^{sgs}\delta_{ij} = -2\mu_t\left(\widetilde{S}_{ij} - \frac{1}{3}\widetilde{S}_{kk}\delta_{ij}\right) \tag{2.80}$$

$$\widetilde{S}_{ij} = \frac{1}{2}\left(\frac{\partial \widetilde{u}_i}{\partial x_j} + \frac{\partial \widetilde{u}_j}{\partial x_i}\right) \tag{2.81}$$

Here, $\widetilde{S}_{ij}$ is the filtered strain rate tensor. We now introduce the transport equation for SGS turbulent kinetic energy. It is given as

$$\frac{\partial}{\partial t}(\bar{\rho} k_{sgs}) + \frac{\partial}{\partial x_j}(\bar{\rho}\widetilde{u}_j k_{sgs}) = -\tau_{ij}^{sgs}\frac{\partial \widetilde{u}_i}{\partial x_j} + \frac{\partial}{\partial x_j}\left(\frac{\mu_t}{Pr_t}\frac{\partial k_{sgs}}{\partial x_j}\right) - C_\varepsilon \bar{\rho}\frac{\partial k_{sgs}^{3/2}}{\overline{\Delta}} \tag{2.82}$$

Here, the three terms on the RHS represent the production, diffusion and dissipation of turbulent kinetic energy, respectively. The production is a source term that increases k_{sgs} by taking the kinetic energy that is dissipated at grid level. The second term represents the diffusion of turbulent kinetic energy where Pr_t is the turbulent Prandtl number. The turbulent Prandtl number compares the transport of energy by momentum diffusivity to that of thermal diffusivity [37]. It is given as

$$Pr_t = \frac{\mu_t C_p}{\lambda} \tag{2.83}$$

The third term in Eq. (2.82) acts as a sink and represents the amount of turbulent kinetic energy that is dissipated per unit time. The expression given as dissipation can be derived by knowing that it scales with the square of the velocity divided by time. Using dimensional analysis, we can show that the dissipation of SGS turbulent kinetic energy, ε_{sgs}, has the form

$$\varepsilon_{sgs} \sim \frac{\mathcal{U}^2}{\mathcal{T}} \sim \frac{\mathcal{U}^3}{\mathcal{L}} \sim \frac{(k_{sgs}^{1/2})^3}{\overline{\Delta}} \tag{2.84}$$

We can therefore introduce a proportionality constant, C_ε, and express the SGS dissipation as

$$\varepsilon_{sgs} = C_\varepsilon \frac{k_{sgs}^{3/2}}{\overline{\Delta}} \tag{2.85}$$

The dynamic aspect of this turbulence model refers to the treatment of the model coefficients, C_k and C_ε. For this we use the concept of scale similarity which assumes that the SGS stresses are controlled by the largest unresolved structures, which are in turn controlled by the smallest resolved structures [37]. By applying a test filter that is larger than the grid filter, we can separate the scales and gain information about how the smallest large–scale stresses relate to the largest small–scale stresses. We use this information to update the model coefficients dynamically, instead of having to prescribe a constant value from the outset. Therefore, we are not forced to adopt the assumption of local equilibrium which is necessary when using other similar one–equation turbulence models.

Local equilibrium requires that the production and dissipation terms given in Eq. (2.82) are perfectly balanced. This does not account for the different conditions between large and small–scale turbulence because the model constants are set as fixed values. It is undesirable to have the relative amounts of production, diffusion and dissipation treated identically across all scales of the flow. The dynamic model is not restricted in this way and we gain information about the history and nonlocal effects of the transport of SGS turbulent kinetic energy [62].

The model coefficients are obtained via the procedure described in detail by Kim [62]. The following is a brief description of the main steps. The test filter, $\widehat{\Delta}$, is taken to be twice the size of the grid filter such that $\widehat{\Delta} = 2\overline{\Delta}$. It is applied to the governing equations after the Favre filter has been applied, and the procedure is the same as it was for the SGS stresses. We define the *subtest* scale stresses as

$$T_{ij} \equiv \bar{\rho}(\widehat{\widetilde{u_i u_j}} - \widehat{\widetilde{u}}_i \widehat{\widetilde{u}}_j) \tag{2.86}$$

The filtered subgrid stresses are then subtracted from the subtest stresses to give the Leonard stresses, L_{ij}. The Leonard stresses represent stresses acting on length scales between that of the grid scale and the test scale. They are given in a form analogous to Eq. (2.80).

$$T_{ij} - \widehat{\tau_{ij}^{sgs}} = \bar{\rho}\Big(\widehat{\widetilde{u_i u_j}} - \widehat{\widetilde{u}}_i \widehat{\widetilde{u}}_j\Big) - \bar{\rho}\Big(\widehat{\widetilde{u_i u_j}} - \widehat{\widetilde{u}_i \widetilde{u}_j}\Big) \tag{2.87}$$

$$L_{ij} \equiv \bar{\rho}\Big(\widehat{\widetilde{u}_i \widetilde{u}_j} - \widehat{\widetilde{u}}_i \widehat{\widetilde{u}}_j\Big) \tag{2.88}$$

$$L_{ij} - \frac{1}{3}L_{kk}\delta_{ij} = -C_k M_{ij} \tag{2.89}$$

$$M_{ij} = 2\widehat{\Delta}\, k_{test}^{1/2}\, \widehat{\widetilde{S}}_{ij} \tag{2.90}$$

Next, we move the RHS of Eq. (2.89) to the LHS, take the square and let the resulting expression be $\mathcal{L}$. $\mathcal{L}$ may be considered a function in terms of C_k. By differentiating $\mathcal{L} = \mathcal{L}(C_k)$ and solving for C_k, we obtain the local minimum value which corresponds to its least square error.

$$\mathcal{L}(C_k) = \Big(L_{ij} - \frac{1}{3}L_{kk}\delta_{ij} + C_k M_{ij}\Big)^2 \tag{2.91}$$

$$\frac{\partial \mathcal{L}}{\partial C_k} = 0 \tag{2.92}$$

$$C_k = \frac{\widehat{L_{ij} L_{ij}}}{M_{ij} M_{ij}} \tag{2.93}$$

We now have a known value for the model coefficient C_k which directly relates the resolved stresses at subtest level to the unresolved stresses at subgrid level. A similar process is repeated to determine the dissipation constant C_ε in Eq. (2.82). These model constants are adjusted with each timestep and provide an improved representation of the SGS stresses. Once both constants are known, we can solve the k_{sgs} transport equation to obtain the SGS turbulent viscosity, leaving us with enough information to close the filtered transport equation for the conservation of momentum, Eq. (2.73)

The turbulent viscosity is also used to solve the remaining unclosed filtered equations. The unresolved energy flux term in Eq. (2.74) is modelled as

$$\bar{\rho}(\widetilde{u_j h_s} - \widetilde{u}_j \widetilde{h}_s) = -\frac{\mu_t C_p}{Pr_t}\frac{\partial \widetilde{T}}{\partial x_j} \tag{2.94}$$

Here, Pr_t is the turbulent Prandtl number. The unresolved species flux term in Eq. (2.75) is modelled as

$$\bar{\rho}(\widetilde{u_j Y_k} - \widetilde{u}_j \widetilde{Y}_k) = -\frac{\mu_t}{Sc_t}\frac{\partial \widetilde{Y}_k}{\partial x_j} \tag{2.95}$$

Here, Sc_t is the turbulent Schmidt number.

Thickened Flame Model

Premixed turbulent combustion flames are characterised by a thin flame front that propagates through the mixture at a specific burning velocity. Predicting the small–scale flame dynamics is an important part of the modelling process. Complications arise because the width of the flame front is often much smaller than the size of a computational grid cell. The thickened flame model [40] (TFM) provides an elegant solution to this problem by artificially thickening the flame so that it can be tracked and resolved at the grid level. If the relative thickness of the flame front is increased, the wider flame body will generally become less sensitive to turbulence. The TFM model compensates for this by introducing an efficiency function that increases the reaction rate. We will first review the fundamentals of *laminar* premixed combustion, in order to set the stage for implementing the TFM in a turbulent system.

The internal structure of a laminar flame front can be divided into separate zones that have certain characteristics. Figure 2.5 illustrates how each zone affects the local mixture composition as the front propagates into the unburnt gas. The two zones of interest are called the preheat zone and the reaction zone, denoted by II and III, respectively. Note that the regions I and IV do not represent zones of the front. They indicate regions that contain either entirely unburnt gas or entirely burnt gas, and are included to assist with the discussion.

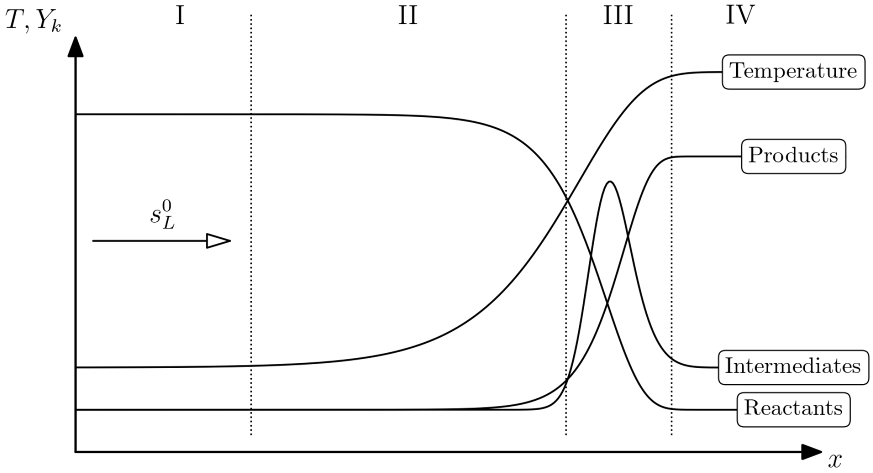

Figure 2.5: *Temperature and species profile of a premixed laminar flame front.*

The preheat zone is characterised by a steady intake of unburnt gas from region I, where the gas mixture is assumed to consist of reactant species at ambient pressure and temperature. A defining feature of the preheat zone is its temperature profile, as shown in Figure 2.5. Heat is transported into the preheat zone from the reaction zone through diffusion. The temperature of the flow increases slowly as it enters region II, yet the rate of temperature increase becomes greater as it approaches region III. Negligible heat is produced inside the preheat zone, since the temperature is not high enough for the unburnt species to react. The initial decline in the mass fraction of the reactants seen in Figure 2.5 is a result of mass diffusion into the reaction zone [63]. Once the flow reaches the interface between II and III, it has been heated to the point of ignition. The flow then exits the preheat zone and enters into the reaction zone.

The chemical reactions start immediately inside the reaction zone. Heat is released and the unburnt reactants are consumed on fast chemical timescales. In Figure 2.5 we can see how the intermediate species are rapidly created and destroyed as the flow passes through region III. Notice that there are some intermediate species remaining in the flow as it enters region IV. These particular species are typically involved in three–body recombination reactions that require a much longer residence time to reach chemical equilibrium [63]. As the temperature of the gas mixture increases, its density also decreases. From continuity we can deduce that the velocity of the burnt mixture is therefore greater than the velocity of the unburnt mixture.

The laminar flame speed, s_L, is considered to be the most important quantity in premixed combustion [64]. From established theories of premixed flames [48], the laminar flame speed is related to the mass diffusivity such that

$$s_L \propto \sqrt{\frac{D}{\tau_c}} \tag{2.96}$$

Here, τ_c is the characteristic timescale of the reaction rate. For a one–dimensional *planar* laminar flame that is propagating freely, such as the example given in Figure 2.5, the flame speed is written as s_L^0 and is used as the standard reference speed for combustion studies. We must also quantify the thickness of the flame before we can determine how it can be modelled within the constraints set by the computational grid resolution. There are several ways to calculate the flame thickness, depending on how much of the front is relevant to the analysis. The *thermal thickness* is commonly used for this purpose [37]. It defines the thickness of the flame front according to the gradient of the temperature curve. This region generally includes the bulk of the reaction zone and a small part of the adjacent preheat zone. With this we define the laminar flame thickness as

$$\delta_L^0 = \frac{T_b - T_u}{\max\left(\left|\frac{\partial T}{\partial x}\right|\right)} \tag{2.97}$$

Here, T_u is the temperature of the unburnt gas and T_b is the temperature of the burnt gas. In Figure 2.5, T_u and T_b correspond to the temperature of the flow in regions I and IV, respectively. We can now take the concept of flame speed and flame thickness and see what happens when turbulence is introduced.

Compared to laminar flames, turbulent flames are a very different animal. We encounter familiar difficulties that arise from the same characteristic features found in other turbulent phenomena. Namely, the transport properties of turbulent flames are defined as functions of the *flow* and not as functions of the *fluid* [65]. On that note, it is useful to investigate the nature of turbulence–chemistry interactions by using dimensionless numbers to see how certain system variables scale with respect to one other. This is analogous to Reynolds scaling in conventional hydrodynamics. Here we adopt a similar approach, but use system variables relevant to turbulent combustion, such as the flame speed and flame thickness. We can assess which quantities dominate at different scales to provide qualitative information about the combustion regime. The TFM model operates on a similar principle. As the thickness of the flame is increased, the TFM dynamically scales other quantities accordingly and the combustion dynamics are maintained as if the flame had never been thickened in the first place. To demonstrate this we need to define the turbulent flame speed and thickness.

Different theoretical models that each use different formulations of the turbulent flame speed, s_T, have been shown to agree with experiment [65]. However, these flame speed correlations that give reliable predictions in one study are far less accurate when tested under different circumstances. It seems the practical use of any one definition of s_T is limited to a narrow range of specific system configurations. Gouldin [66] calls the turbulent flame speed an "ill–defined quantity." In any case, the ideal definition is not relevant here. The current understanding of turbulent flames is built upon the foundational work of Damköhler [67], where s_T can be given in the form

$$\frac{s_T}{s_L} = 1 + \alpha\left(\frac{u'_{\text{rms}}}{s_L}\right)^n \tag{2.98}$$

Here, α and n are model constants and u'_{rms} is the RMS of the velocity fluctuations. The thickness of a turbulent flame depends on the width of the flame *brush*, which is rapidly fluctuating on account of the turbulence. The width of the *instantaneous* flame brush corresponds to the maximum amplitude of these fluctuations. The instantaneous reaction zone is assumed to propagate locally in the normal direction with a velocity equal to the laminar flame speed. The thickness of the turbulent flame brush, δ_T, is assumed to be on the order of the integral length scale and can be estimated as

$$\delta_T \approx \frac{\nu}{s_L^0} \tag{2.99}$$

Here, ν is the kinematic viscosity of the flow. For most premixed flames the mean reaction zone thickness, δ_r, is approximately an order of magnitude smaller than the width of the flame front [37].

Since we are dealing with multi-scale phenomena it helps to examine how the turbulence–chemistry interactions are different across the range of scales in question. Figures 2.6 and 2.7 illustrate how the structure of the flame is affected by different flow conditions. The turbulent length scales are represented by ℓ_0 on the largest scale, ℓ_t on the integral scale and ℓ_η on the Kolmogorov scale.

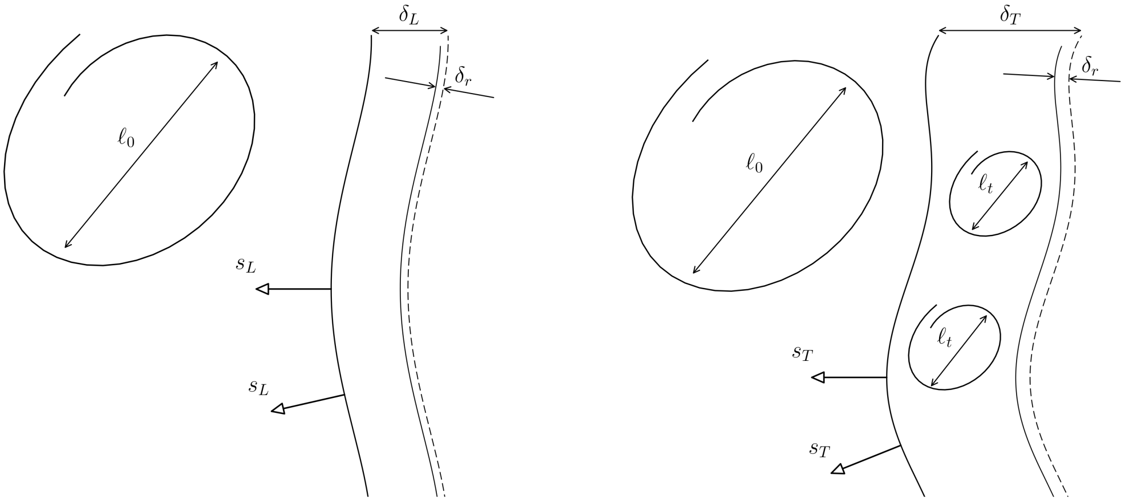

(a) *Mild turbulence conditions.* (b) *Moderate turbulence conditions.*

Figure 2.6: *Structure of a premixed flame.*

Large–scale turbulence can be several orders of magnitude greater than the size of the chemical scales. In this case, the relationship between turbulence and the flame is entirely kinematic and only the large–scale structure of the flame is influenced, as shown in Figure 2.6a. Eddies on this scale will alter the surface geometry causing the flame to wrinkle, but do not have sufficient intensity to disturb the chemistry. The internal flame structure remains intact and behaves just as it would under laminar flow conditions where the mixing is entirely governed by mass diffusion. If the flow becomes more turbulent the flame dynamics become more complex. On smaller levels, the turbulent scales and the chemical scales can eventually converge and a two–way interaction develops. When the turbulent motions are acting on scales smaller than the size of the flame, eddies can enter the preheat zone, as seen in Figure 2.6b. Velocity fluctuations distort the flame structure from the inside out, enhancing the mixing process and increasing the total surface area of the front. This increases the consumption rate of reactant species and results in a thickening of the overall flame body. These effects are compounded as the flow becomes more and more turbulent. Figure 2.7 shows how the inner flame is affected by the Kolmogorov scale eddies, which can become small enough to enter the reaction zone. Ultimately, the turbulence may get too disruptive for the reactions to proceed effectively, undermining the entire combustion process.

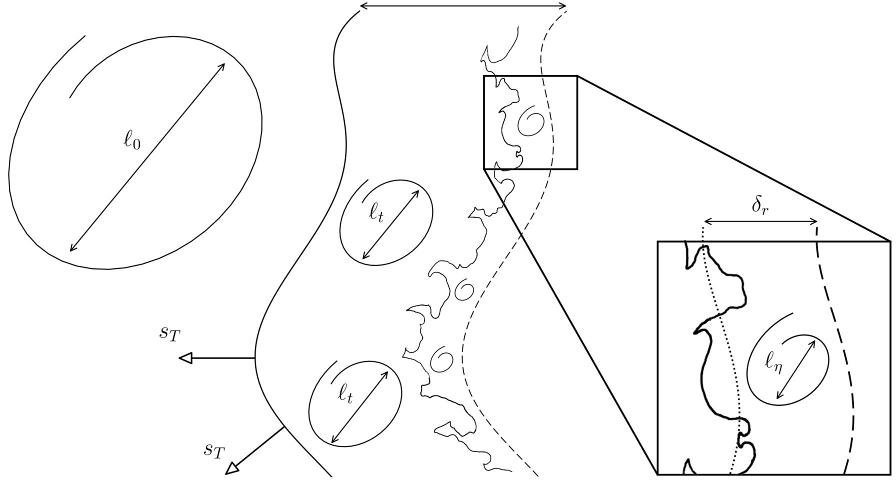

Figure 2.7: *Structure of a premixed flame in high turbulence conditions.*

Different combustion regimes are produced under different flow conditions with different mixture compositions. Certain regimes are more or less favourable depending on the particular application. Here we introduce two non–dimensional numbers that are used to describe the type of combustion regime that a particular set of conditions may produce.

The turbulent Damköhler number, Da, is used to quantify how the reaction rate is influenced by the interactions between large–scale turbulence and chemistry. It can be expressed as

$$Da = \frac{\tau_t}{\tau_c} = \frac{(\ell_t / u_t)}{(\delta_L^0 / s_L^0)} \tag{2.100}$$

Here, τ_t is the integral timescale and τ_c is the chemical timescale. The integral timescale for the large turbulent eddies is estimated as the ratio of the integral length scale, ℓ_t, to the corresponding integral velocity scale, u_t. The chemical timescale represents the time required for the front to travel a distance equal to the flame thickness, δ_L^0, while moving at the laminar flame speed, s_L^0. For very large Damköhler numbers there is little interaction between the largest eddies and the flame front due to the large disparity between scales. When $Da \gg 1$ the overall reaction rate is governed by mass diffusivity and flame mobility is limited by the local laminar flame speed. The influence of turbulence on the reaction rate is negligible. If the integral scales become comparable to the chemical scales, larger eddies will enhance the global mixing process and cause the surface wrinkling to become more pronounced. For $Da \approx 1$ the turbulent convection can replenish burnt product species with unburnt reactant species at the same rate they are being consumed. Here, the reaction rate is controlled by a balance of convection and mass diffusion. When $Da < 1$ the turbulent activity begins to dominate the mixing process and the flame wrinkling intensifies. If $Da \ll 1$ the mixture content is continuously restocked with fresh reactant species much faster than they are consumed. The combustion process is only limited by the rate that the chemical reactions can burn through the reactants. This is known as the *perfectly stirred reactor* [37].

A combustion regime is classified on the smallest scales by using the Karlovitz number, Ka. In contrast to the Damköhler number, which is used for large–scale turbulence, the Karlovitz number relates the chemistry scales of the flame to the Kolmogorov scales of the turbulence. It can be expressed as

$$Ka = \frac{\tau_c}{\tau_\eta} = \sqrt{\frac{\delta_L^0}{\ell_\eta}\left(\frac{u_\eta}{s_L^0}\right)^3} = \frac{\delta_L^0}{s_L^0}\sqrt{\frac{\varepsilon}{\nu}} \tag{2.101}$$

Here, τ_η, ℓ_η and u_η are the respective time, length and velocity scales associated with Kolmogorov turbulence, ν is the kinematic viscosity and ε is the dissipation rate of turbulent kinetic energy. The Karlovitz number is a measure of how much the inner flame is disturbed by the smallest eddies of the flow. If $Ka < 1$ the small–scale turbulence has no effect on the inner structure of the flame and even the tiniest eddies cannot penetrate the flame front. The flame front behaves as it would under laminar conditions where the propagation rate is governed by mass diffusivity. If $Ka > 1$ the small eddies start to occupy the preheat zone and the local reaction rate is controlled by both chemical diffusion and turbulent mixing. The edge of the reaction zone can become highly wrinkled, but it remains intact. Chemical processes inside the reaction zone are still mostly unaffected and the flame front maintains its overall laminar behaviour. If $Ka \gg 1$ the small–scale eddies are able to penetrate the reaction zone and drastically transform the flame structure. Turbulent mixing dominates the reaction rate and the front is no longer considered a laminar structure. The reaction progress is also altered by the removal of intermediate species from the reaction zone. This can lead to local extinction and the combustion process may leave a considerable amount of unburnt reactant and radical species in its wake. Global extinction of the flame will occur if the turbulence intensity becomes too great.

Figure 2.8 shows how the length and velocity scales can indicate which type of combustion regime may be expected. This is called a Borghi Diagram [68] and is presented here in classical form. Note that modified versions of the Borghi Diagram, that consider different flame and flow variables, can also be used to characterise premixed turbulent combustion regimes [65]. Region I is for purely laminar flames and is of little relevance to this discussion. Region II is the *wrinkled flamelet regime*, where the flame travels faster than even the largest eddies. Turbulent fluctuations result in surface wrinkling, but have negligible effect on the combustion dynamics. Region III is called the *corrugated flamelet regime*, which differs from region II since $u_t > s_L^0$. Eddies can alter the overall geometry of the flame and enhance the wrinkling effect, but the flame structure is preserved. Things become more interesting once we enter region IV where $Ka > 1$. This is known as the *distributed reaction zone* or the *thickened–wrinkled flame regime* and is where turbulence begins to assert its influence on combustion. Kolmogorov scale eddies are now smaller than the global flame thickness and can

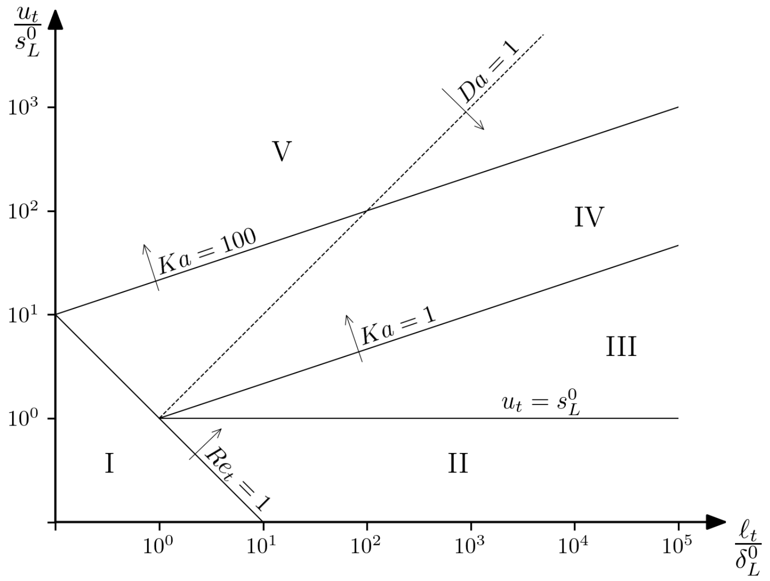

Figure 2.8: *Premixed turbulent combustion regimes.*

enter the preheat zone. The fluctuating motions modify the inner structure, causing the global flame thickness to increase as the turbulent flame brush develops. The Kolmogorov scale eddies are still larger than the thickness of the reaction zone, which behaves more like a wrinkled laminar reaction zone. Region V is called the *broken reaction zone* or the *thickened flame regime.* This is the point at which the Kolmogorov eddies are small enough to enter the reaction zone, causing it to thicken in a similar way to that of the preheat zone region IV. The transition into region V generally occurs at $Ka \approx 100$ [37]. As turbulence increases, eddies of greater intensity are able to infiltrate the inner flame and disturb the reaction zone. Progress along the chemical pathway is interrupted as intermediate species are displaced out of the reaction zone via rapid small scale convective motions. The reaction faces the risk of local extinction, with the possibility of global flame extinction becoming increasingly likely.

Now we can introduce the TFM. As shown by Colin et al. [40], the laminar flame thickness and the laminar flame speed relate to the mass diffusivity and the reaction rate as follows

$$\delta_L^0 \propto \frac{D}{s_L^0} \tag{2.102}$$

$$s_L^0 \propto \sqrt{D\dot{\omega}} \tag{2.103}$$

Next we introduce a thickening factor, $\mathcal{F}$, and use it to scale up δ_L^0 in Eq. (2.102). By imposing the constraint that the laminar flame speed should remain constant when the flame is thickened, we obtain the following relation

$$\mathcal{F}\delta_L^0 \propto \frac{\mathcal{F}D}{s_L^0} \tag{2.104}$$

$$s_L^0 \propto \frac{\sqrt{\mathcal{F}}}{\sqrt{\mathcal{F}}}\sqrt{D\dot{\omega}} = \sqrt{(\mathcal{F}D)(\dot{\omega}/\mathcal{F})} \tag{2.105}$$

This shows that the mass diffusivity should be increased by multiplying D with $\mathcal{F}$, and that the reaction rate should be decreased by dividing $\dot{\omega}$ with $\mathcal{F}$. Notice that we have not changed the value of s_L^0. For a turbulent flame, the motion of the flame front is governed by both diffusion and convection, so it follows that we have artificially enhanced the contribution of diffusion at the expense of turbulence. This alters the turbulence–chemistry interaction and may change the entire combustion regime if left unchecked.

Fortunately, we can also modify the speed of the flame such that the extra thickness is maintained while the other flame properties are simultaneously restored to their pre–thickening state. This is done by introducing another parameter called the efficiency function, $\mathcal{E}$. Now taking the flame speed expression from Eq. (2.103), we scale s_L^0 by $\mathcal{E}$ to give

$$\mathcal{E}s_L^0 \propto \mathcal{E}\sqrt{D\dot{\omega}} = \sqrt{(\mathcal{E}D)(\mathcal{E}\dot{\omega})} \tag{2.106}$$

By increasing the flame speed we are strengthening the wrinkling effect without affecting the rest of the flame. We can consider $\mathcal{F}$ and $\mathcal{E}$ to be ratios of the turbulent flame properties to the laminar flame properties. This way we can see how Da from Eq. (2.100) is suitably changed and the desired level of turbulence–chemistry interaction is achieved.

$$Da = \frac{(\ell_t/u_t)}{(\mathcal{F}\delta_L^0/\mathcal{E}s_L^0)} = \frac{(\ell_t/u_t)}{(\delta_T/s_T)} \tag{2.107}$$

$$\mathcal{F} = \frac{\delta_T}{\delta_L^0}\,, \quad \mathcal{E} = \frac{s_T}{s_L^0} \tag{2.108}$$

Here, δ_T and s_T are the turbulent flame thickness and turbulent burning velocity, respectively. These changes are introduced to the species transport equation by modifying the diffusion and reaction rate terms. Poinsot and Veynante [37] give the following expression that summarises the implementation of the TFM:

$$\begin{array}{rlll} \text{Diffusivity:} & D & \xrightarrow{\text{Thickening}} \mathcal{F}D & \xrightarrow{\text{Wrinkling}} \mathcal{E}\mathcal{F}D \\ \text{Reaction rate:} & \dot{\omega} & \xrightarrow{\text{Thickening}} \dot{\omega}/\mathcal{F} & \xrightarrow{\text{Wrinkling}} \mathcal{E}\dot{\omega}/\mathcal{F} \end{array}$$

The values for $\mathcal{F}$ and $\mathcal{E}$ are computed and updated dynamically using an efficiency function described by Wang, Boileau and Veynante [69].

3 Method

3.1 Bluff Body Configuration

The AFRL bluff body stabilised combustor was built by the United States Air Force Research Laboratory to perform premixed turbulent combustion experiments related to aircraft propulsion systems [38][43]. The combustion dynamics of phenomena such as lean blow–off and thermo–acoustic instabilities can be observed and measured. Test data can then be used to validate numerical models and improve their predictive capability. The entire AFRL rig is a large experimental arrangement that includes upstream plenum sections where the fuel and air is injected and conditioned. The flow is directed into the combustion chamber test section where it is ignited and measurements are recorded. Exhaust gasses exit the test section into atmospheric pressure. This thesis only considers the test section of the AFRL combustor.

The test section is a rectangular duct that houses a bluff body, which is used to anchor the flame. The bluff body, also called the *flame holder*, is an equilateral triangle that spans the width of the combustion chamber and lies downstream of the inlet at approximately 18% of the total combustion chamber length. The forward tip (apex) of the triangle points directly upstream and is located at the midpoint of the chamber height. Once the gas is ignited, the flame is stabilised at the trailing edge (base) of the bluff body and the exhaust exits the outlet, passing into atmosphere. Here, we are modelling the combustion chamber according to the MVP workshop specifications [41]. The geometry of the model combustion chamber is illustrated in Figure 3.1.

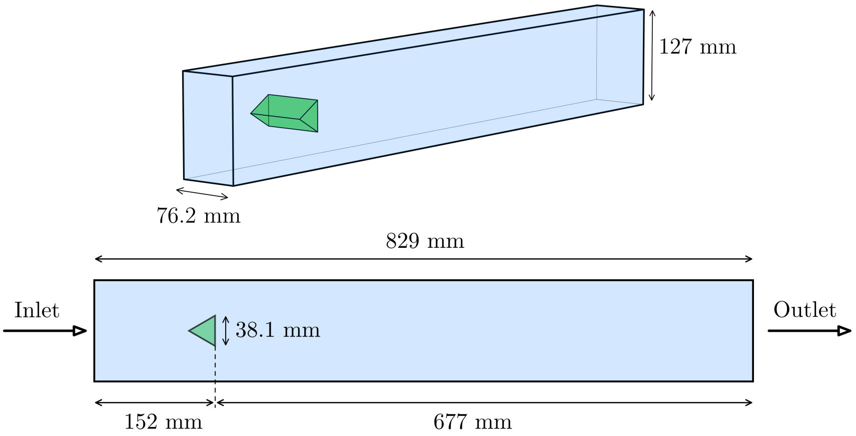

Figure 3.1: *Model combustion chamber size specifications. The green triangular prism is the flame holder.*

3.2 Software Evaluation

Two different commercial software packages were considered for the analysis. They were ANSYS Fluent and Siemens Simcenter STAR–CCM+. A number of test cases were performed with both software packages to assess their strengths and weaknesses before deciding which to use for the final analysis. The test cases considered aspects such as software features, numerical stability, computational expense and overall model performance.

LES models for propane combustion with the Ghani reaction mechanism were built using Fluent and STAR–CCM+ according to the MVP case specifications. The Fluent model used a pressure–based solver with the PISO scheme, the dynamic SGS kinetic energy model and the TFM. The stiff chemistry solver was disabled for FRC which implies that the reaction rate source term is included explicitly in the species transport equation. The non–reflecting acoustic wave model was enabled for the pressure outlet boundary conditions. The STAR–CCM+ model used the segregated flow solver with the PISO scheme, the dynamic Smagorinsky SGS model and the TFM. The stiff chemistry solver was used to compute the chemical source term. A reflecting boundary, that behaves like an acoustically rigid interface, was used for the pressure outlet because non–reflecting boundary conditions were not available with the segregated flow solver in STAR–CCM+.

The LES study presented by Fureby [44] was used as a benchmark to determine which software package would be preferred for modelling premixed turbulent combustion in the AFRL combustor. The decision ultimately came down to the observed behaviour of the TFM and treatment of the chemical source term. Note that the chemical source term refers to the filtered reaction rate variable $\overline{\dot{\omega}}_k$, featured in Eq. (2.75). The STAR–CCM+ model was found to give unusually high values for the TFM parameters. Most notably, the efficiency function was approximately five times larger than expected. The Fluent model, on the other hand, provided more agreeable results for the same TFM quantities.

Recall that the efficiency function is a vital component of the TFM and is applied directly to the reaction rate term, as per Eq. (2.106). Note that the reaction rate term contains the highly non–linear rate constant, as discussed in Section 2.2.3. In the Star–CCM+ model, the reaction rate is obtained with an operator splitting algorithm that solves the timestep integral by finding average reaction rates to reduce stiffness [70]. In contrast, the reaction rate was computed explicitly in the Fluent model, which did not appear to have any difficulty in doing so, despite the stiff equations. The splitting error introduced by the STAR–CCM+ stiff chemistry solver may have contributed to the discrepancies observed in the TFM results. Attempts to optimally configure the complex chemistry model used by STAR–CCM+ were unsuccessful within the allocated time frame. It was concluded that Fluent had performed better in this particular case and would therefore be used for the primary CFD analysis.

3.3 Numerical Setup

3.3.1 Reaction Mechanism

The physical properties of the fluid are set by importing the reaction mechanism. Fluent reads this in the form of a CHEMKIN data file [71]. Propane combustion was modelled using the semiglobal Ghani mechanism and hydrogen combustion was modelled using the skeletal Z22 mechanism. Further details of these reaction mechanisms are listed in Table 3.1. The thermochemical properties of the mixture are contained in three different sections of the CHEMKIN file. The reactions section contains the chemical equations for all of the elementary reactions. The Arrhenius quantities A_j, β and E_A, that are required for Eq. (2.49) are also included in the reactions section. The thermodynamics section contains the NASA–7 coefficient data for the specific heat polynomials of each chemical species. The transport section contains additional details of the physical properties of each species. The transport data relates to molecular geometry, Lennard–Jones potential, particle collisions and polarisability [72], which is used when computing the equations of kinetic theory that were given in Section 2.1.2. Preliminary calculations were done prior to starting the CFD simulations to verify that the species properties used by Fluent matched up with the values in the reaction mechanism. A direct visual check of the numbers can be tricky since the CHEMKIN data file is not a convenient read and many of the values are listed in a system of units that are different to the corresponding units used by Fluent. The Python package Cantera [73] was used to convert the CHEMKIN file into Cantera format so that all the necessary quantities could be changed into SI units and easily compared.

Mechanism	Classification	Fuel type	Reactions	Species
Ghani [42]	Semiglobal	C_3H_8	2	6
Z22 [45]	Skeletal	H_2	22	9

Table 3.1: Chemical reaction mechanism details.

3.3.2 Mesh

Each simulation case was performed on two different grids. The coarse grid consisted of approximately 8.02×10^5 computational cells with an average cell–size of 1.7 mm and the fine grid consisted of approximately 3.67×10^6 computational cells with an average cell–size of 1.0 mm. The two grids are geometrically similar and built from structured hexahedral elements. The overall structure of the mesh can be seen in Figure 3.2.

At the flame holder, notice that the average cell–size is reduced along the mid–section in front of the stagnation point, and also directly downstream of the upper and lower trailing edges. The latter is of particular importance in this case, since the finer grid resolution helps to capture the small–scale processes and large flow gradients that occur in this region. Due to the flow separation, a shear layer will develop here and start to generate vortices, which will be consecutively released from one trailing edge followed by the other trailing

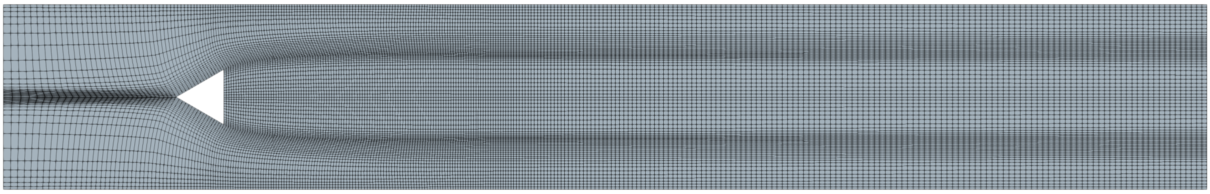

Figure 3.2: *Mesh structure of the combustion chamber.*

edge, in ongoing succession. Although the flame body is always rapidly moving and changing shape, it remains anchored to the rear surface of the flame holder. On average, we can expect the front of the flame to extend downstream along the lines of where the smaller grid elements are positioned. The mesh has a reflective symmetry along the horizontal mid plane and a translational symmetry along the vertical mid plane.

3.3.3 Model Configuration

The numerical models are built over three main stages that are described below. The full procedure for constructing and solving a CFD model was automated with a Fluent journal file, which started at the bare mesh and finished once enough transient data had been recorded from a complete working model. By scripting all setup and run instructions as a sequence of text commands, the CFD models were able to be constructed quickly and consistently without manual intervention through the Fluent GUI.

Setup Stage 1

First, a nonreacting flow field is generated by running a steady–state, Reynolds Averaged Navier Stokes (RANS) simulation. Fluent uses various methods to compute the different physical properties of each chemical species based on the input data from the reaction mechanism. Kinetic theory is used for both viscosity and thermal conductivity, and piecewise polynomials are used for the specific heat. The remaining species' quantities are constants that are taken from the mechanism data. The collective mixture properties are computed by Fluent according to the individual properties of each species. Density uses the ideal gas law, mass diffusivity uses kinetic theory and specific heat, thermal conductivity and viscosity use the mixing law.

All models used a pressure–based solver. The two–equation standard k–ε model [74] is used for the steady–state simulation. The settings for Standard Wall Function, Viscous Heating, Compressibility Effects and Production Limiter are all activated. Adiabatic, no–slip boundary conditions are applied to the upper and lower walls and to the flame holder, which are highlighted in Figure 3.3a. The two side walls highlighted in Figure 3.3b are set as a pair of translational periodic matching interfaces. The inlet and outlet boundaries are highlighted in Figures 3.3c and 3.3d, respectively. The inlet boundary is set as a mass–flow inlet with a total temperature of 310 K. The mass flow rate, species mass fractions and turbulence parameters are set differently, depending upon the type of fuel used. Cantera was used to compute the required mass fractions for each value of ϕ. The values for propane and hydrogen are given in Table 3.2.

Fuel	ϕ	$\dot{m}$ $[{}^{\mathrm{kg}}/{}_{\mathrm{m}^3}]$	Y_{fuel}	Y_{O_2}	k $[{}^{\mathrm{m}^2}/{}_{\mathrm{s}^2}]$	ε $[{}^{\mathrm{m}^2}/{}_{\mathrm{s}^3}]$
C_3H_8	0.650	0.18190	0.0400704	0.2236708	0.118	0.210
H_2	0.406	0.23878	0.0117840	0.2302617	0.098	0.158

Table 3.2: Inlet boundary conditions.

The outlet boundary is set as a pressure outlet with the backflow pressure specification set to total pressure and the backflow total temperature set to 300 K. In all cases, the fuel content of the mixture is assumed to have been entirely consumed by the time the flow exits the domain. All species mass fractions are set to zero at the outlet except for oxygen which is set at $Y_{\mathrm{O}_2} = 0.223671$. The input values for the RANS turbulence quantities k and ε are set for an inflow turbulence intensity, I, of approximately 1%, and were calculated as follows

$$I \equiv \frac{u'_{\mathrm{rms}}}{U_0} = 0.16 Re^{-1/8} \tag{3.1}$$

$$k = \frac{3}{2}(I U_0)^2 \tag{3.2}$$

$$\varepsilon = 0.09^{3/4} \frac{k^{3/2}}{\ell_t} \tag{3.3}$$

Here u'_{rms} is the RMS of the velocity fluctuations and U_0 is free stream flow velocity at the inlet.

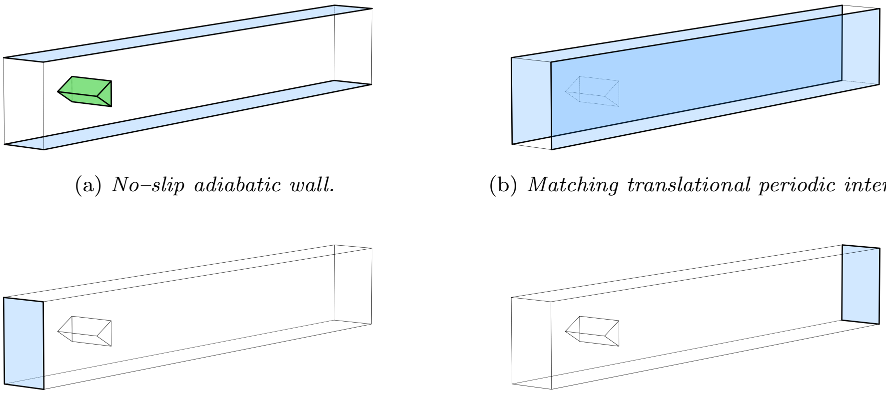
(a) *No–slip adiabatic wall.* (b) *Matching translational periodic interface.*

(c) *Mass–flow inlet.* (d) *Pressure outlet.*

Figure 3.3: *Inlet and outlet boundary conditions.*

The RANS model uses a coupled solver which updates the pressure and velocity fields simultaneously. The spatial discretisation schemes for density, momentum, energy and species are second–order upwind, and the two RANS quantities, k and ε, both use first–order upwind schemes. The under–relaxation factor for density is 0.25. The under–relaxation factor for both pressure and momentum is 0.5. Species, energy, k and ε all have an under–relaxation factor of 0.75. The automatic method is used to determine step size of the steady–state solver iterations. Fluent computes this based on the time and length scales of the system. The convergence criteria for the mass, momentum, energy, k and ε equations is set at 10^{-7}. The nonreacting steady–state RANS simulation is then solved for 2000 iterations.

Setup Stage 2

Once the stage 1 solution has sufficiently converged, the volumetric reactions are turned on. The Eddy Dissipation Concept (EDC) model is activated to govern the turbulent–chemistry interactions and then the fuel is ignited. Note the simulation remains as a steady–state RANS model throughout stage 2.

The EDC model [75] assumes the chemical reaction rate is governed by the mixing process and that the reactions occur in certain regions of the flow where there is small–scale dissipation of turbulent kinetic energy. The EDC model considers the majority of the flow to be in a nonreacting state, that contains small and spatially isolated reacting zones within it. Since turbulent kinetic energy is dissipated differently by large–scale eddies compared to small–scale eddies, the reacting zones are identified as regions where the turbulent dissipation rate indicates small–scale structures are actively mixing the flow enough to drive the combustion process.

In stage 2, the reaction rate is computed using Fluent's stiff chemistry solver and direct integration. A temporary temperature patch is applied to a small region immediately downstream of the flame holder. The patch is set such that the local temperature is momentarily increased to a value that corresponds to the activation energy of the fuel and will ignite the combustion. The stage 2 simulation then continues to solve for a further 2000 iterations so that the flame body is allowed to develop and the solution re–converge.

Setup Stage 3

The solution state of the combusting RANS model is then used as the initial state of the final LES model. The system is switched into LES mode and the turbulence model is upgraded to the dynamic SGS kinetic energy model with $Pr_t = 0.7$. The EDC model is swapped for the TFM, which requires the laminar flame speed, the laminar flame thickness and the integral length scale of the turbulence as input parameters. Flame speed and flame thickness was computed using Cantera's one–dimensional steady–state freely propagating flame model. The integral length scale for propane combustion was given by Fureby [44] as $\ell_t = 0.003$ m. The integral length scale for hydrogen combustion was estimated using the velocity field of the RANS model and taken to be $\ell_t = 0.001$ m. The specific values for each fuel and the corresponding timestep for the LES time integration scheme are given in Table 3.3.

Fuel	s_L^0 [m/s]	δ_L [m]	ℓ_t [m]	Δt [s]
C_3H_8	0.218	5.283×10^{-4}	0.003	7.50×10^{-6}
H_2	0.335	4.954×10^{-4}	0.001	1.875×10^{-6}

Table 3.3: LES model settings.

The non–reflecting acoustic wave model is applied to the outlet boundary conditions. The momentum equation is solved with a bounded central differencing scheme and the density, energy, species and SGS kinetic energy equations are solved with a second–order upwind scheme. A bounded second–order implicit scheme is used for temporal discretisation and the PISO scheme [76] is used for pressure–velocity coupling. Pressure, density, momentum and SGS kinetic energy all have an under–relaxation factor of 0.9. The under–relaxation factors for energy and species are 0.5 and 0.25, respectively. The timestep used for each fuel type is given in Table 3.3. The system is solved for a minimum simulation time of six complete *flow–throughs*. One flow–through corresponds to the time taken by the fluid to travel along the horizontal axis, from the inlet to the outlet, at a speed equal to the inflow velocity. After three complete flow–throughs had been completed, time series data was extracted from four centrally located recording stations, downstream of the flame holder, as shown in Figure 3.4.

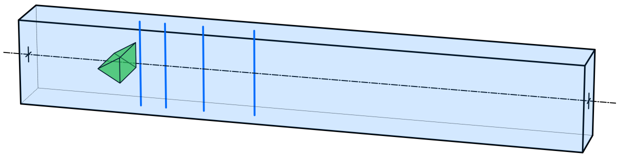

Figure 3.4: *Vertical profile stations (blue) at* $0.5h$, $1.5h$, $3h$ *and* $5h$, *behind the flame holder.*

Starting from the rear surface of the flame holder, the stations are located at $0.5h$, $1.5h$, $3h$ and $5h$, where h is the height of the flame holder. At each station, data was exported every four timesteps for the remaining three flow–throughs. This information is used to generate vertical flow profiles of mean and RMS values for the post processing analysis. Given the time series data for an arbitrary flow variable, φ, the RMS values are computed as

$$\varphi_{\text{rms}} = \sqrt{\langle(\varphi - \langle\varphi\rangle)^2\rangle} \tag{3.4}$$

Here, $\langle\varphi\rangle$ is the arithmetic mean and φ_{rms} is the RMS of the perturbations about the mean.

3.4 Switching to Hydrogen

3.4.1 Matching Variables

A numerical model can only be built if the initial conditions of the system are known. To model hydrogen combustion we must first specify how much fuel is to be injected into the combustor. Therefore, we need an equivalence ratio and a mass flow rate, so that boundary conditions can be set for the inlet. For the propane model, this information was provided by the MVP workshop specifications. No such information is available for a hydrogen model, so an appropriate system configuration had to be determined by other means. The hydrogen model operating conditions listed in Table 3.2 were obtained using the following approach.

If the same values that were used to model propane, where $\phi = 0.65$ and $\dot{m} = 0.1819$ kg/m³, were also used for the hydrogen model, the combustion regime would change considerably and it would be much more difficult to make a meaningful comparison between the two systems. Because H_2 gas has a lower density, the inflow velocity of the unburnt mixture would have to be almost 25% faster to match the same ϕ and $\dot{m}$ used for propane. As a result, when the flow separates from the trailing edge of the flame holder, the vortex shedding would be intensified and have a notable effect the mixing process within the flame. The change in flame speed is even more influential. At $\phi = 0.65$, the laminar flame speed of the hydrogen mixture is over seven times faster than that of the propane mixture. Even with the increased inlet velocity, the flow cannot compete with such a high flame speed. The flame front would advance upstream, against the oncoming flow, and creep towards the inlet. This could have catastrophic consequences in practice.

The ratio of the laminar flame speed to the inflow velocity, s_L^0/U_0, is the first quantity to be matched. If the H_2 mixture and the C_3H_8 mixture have the same value for s_L^0/U_0, the flame front is expected to propagate into the unburnt gas at approximately the same rate for both models. For the propane model this was $s_L^0/U_0 = 0.01312$, where the flame speed was computed with Cantera and the inflow velocity corresponds to the MVP case specifications for the AFRL combustor. Before this can be used to configure the hydrogen model, it is necessary to identify the actual values that give this number. Since both s_L^0 and U_0 are unknown, there are infinitely many ways to divide the former by the latter to obtain a value of 0.01312. A relevant and meaningful combination of s_L^0 and U_0 is needed.

To determine the desired values, we use the *absolute* heat of combustion, Q_{abs}, which is given as

$$Q_{\text{abs}} = Q\dot{m} \tag{3.5}$$

Here, $\dot{m}$ is the mass flow rate and Q is the heat of combustion per unit mass, which was introduced in Eq. (2.29). Cantera is used to compute Q by way of minimising the Gibbs free energy the mixture, as discussed in Section 2.2.2. The absolute heat of combustion represents the total amount of heat released by the reaction per second, and provides a suitable quantity for matching the two combusting systems.

There are a few things to recall if we are to tie this all together:

- The heat of combustion is related to the mass fractions, as per Eq. (2.30).
- The mass fractions of the reactant species determine the equivalence ratio, as per Eq. (2.26).
- The equivalence ratio determines the laminar flame speed via Cantera.
- The mass flow rate and the inflow velocity are related by $\dot{m} = \rho A U_0$, where A is the cross–sectional area of the combustor inlet, shown in Figure 3.3c.

From this we can deduce that for any ϕ and its associated Q, there exists a particular $\dot{m}$ that gives a matching value of Q_{abs}. All combinations of ϕ and $\dot{m}$ that have a matching Q_{abs} can be plotted as a curve. This is illustrated by the blue line in Figure 3.5, where $\dot{m}$ is replaced by U_0, since $U_0 = \dot{m}/(\rho A)$. Furthermore, for any ϕ and its associated s_L^0, there exists a particular U_0 that gives a matching value of s_L^0/U_0. All combinations of ϕ and U_0 that have a matching s_L^0/U_0 can also be plotted as a curve. This is illustrated by the red line in Figure 3.5.

The point at which the blue and red curves intersect specifies the exact values of ϕ and U_0 that the hydrogen model will need, in order to have the same Q_{abs} and s_L^0/U_0 that the propane model has. This provides the desired inflow mixture conditions that are used for the CFD model of premixed hydrogen combustion which is constructed using the procedure described in Section 3.3.3. We have $\phi_{H_2} = 0.4062$ and $\dot{m}_{H_2} = 0.23878$ kg/m³.

3.4.2 Modified Domain

Further changes to the model configuration were needed for the hydrogen case after it was found to produce spurious solutions. Extreme pressure fluctuations developed throughout the domain, as well as large backflow velocities at the outlet. While the hydrogen model is expected to feature much stronger combustion instabilities, the results were deemed unphysical due to pressure field oscillations with amplitudes greater than two standard atmospheres. The non–reflecting acoustic wave model was tested for both inlet and outlet boundaries, but the unwanted pressure modes and backflow velocities could not be eliminated.

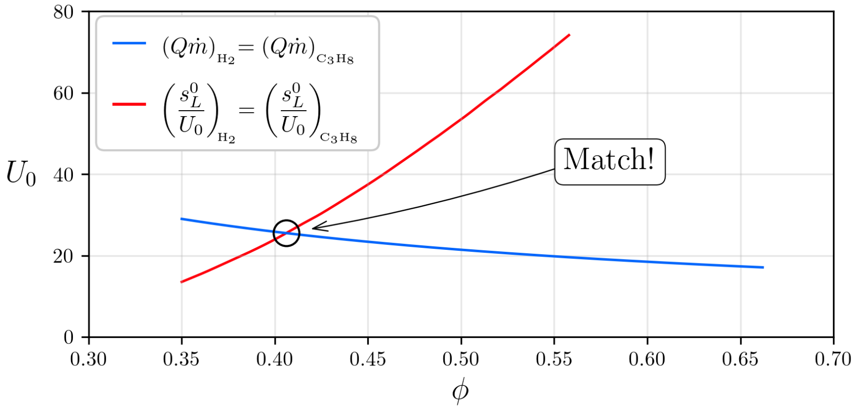

Figure 3.5: *Plotted quantities for the hydrogen model that match those of the propane model.*

A decision was made to expand the computational domain by adding an exhaust region to facilitate the flow of hot gas through the outlet. An extended inlet duct was also included upstream of the flame holder. This isolates the combustion chamber from any false acoustic reflections that may be produced by sensitivities to the imposed boundary conditions at the inlet and outlet.

The mesh structure of the combustion chamber is identical to that of the original domain, while grid stretching is used for the extended regions to minimise computational expense. The larger grid cells will also help to attenuate waves that travel over them, since they dampen fluctuations by producing more numerical dissipation. The extended coarse grid features approximately 1.50×10^6 cells. Modelling hydrogen combustion using a fine grid equivalent could not be achieved within the allocated time frame and has been neglected. The global structure of the extended mesh can be seen in Figure 3.6 where the red box indicates the location of the domain used for the propane model.

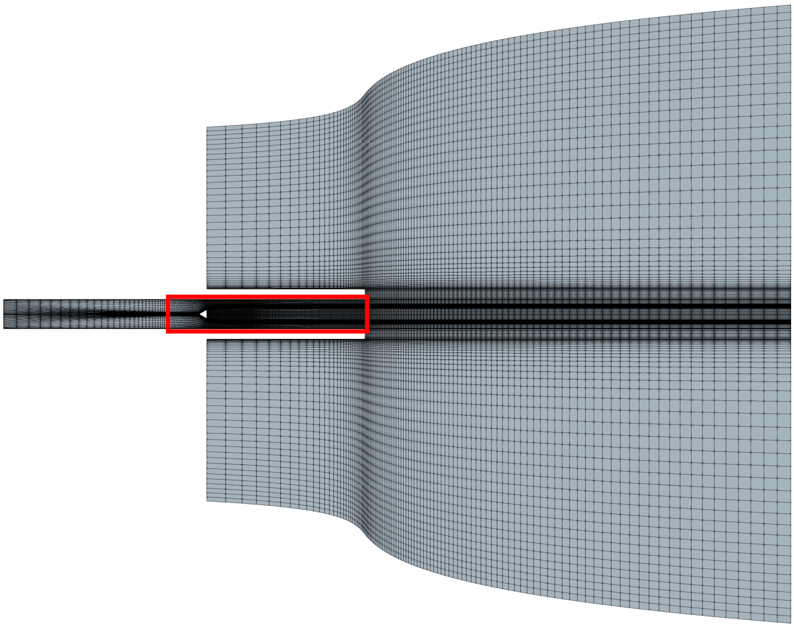

Figure 3.6: *Mesh structure of the expanded domain. The combustion chamber is represented by the red box where the mesh structure is identical to that of the original grid, shown in Figure 3.2.*

The upper and lower boundaries of the exhaust region are set as pressure inlets with a gauge pressure of 0.6 Pa, a total temperature of 300 K and a strictly horizontal flow direction. The non–reflecting acoustic wave model is used for the inlet and the outlet. All other boundary conditions are unchanged. Transient data is still collected from the same locations inside the combustion chamber, as shown in Figure 3.4.

4 Results

The results for both the propane and hydrogen combustion models are presented in this section. All instantaneous results given below are obtained from the end state of the simulation. All transient results are sampled periodically throughout the final three flow–throughs of the simulation. The contour plots use data extracted from the vertical midplane along the central x–axis, such that the plane intersects each profile station seen in Figure 3.4. The two–dimensional plots were all created in Python and the three–dimensional renderings were created using the scientific visualisation software package, Paraview.

4.1 Propane Combustion

Instantaneous contour plots for the propane combustion model are given in Figures 4.1a and 4.1b for the coarse and fine grids respectively. The field variables from top to bottom are temperature, gauge pressure, the horizontal velocity component and the y gradient of the horizontal velocity component.

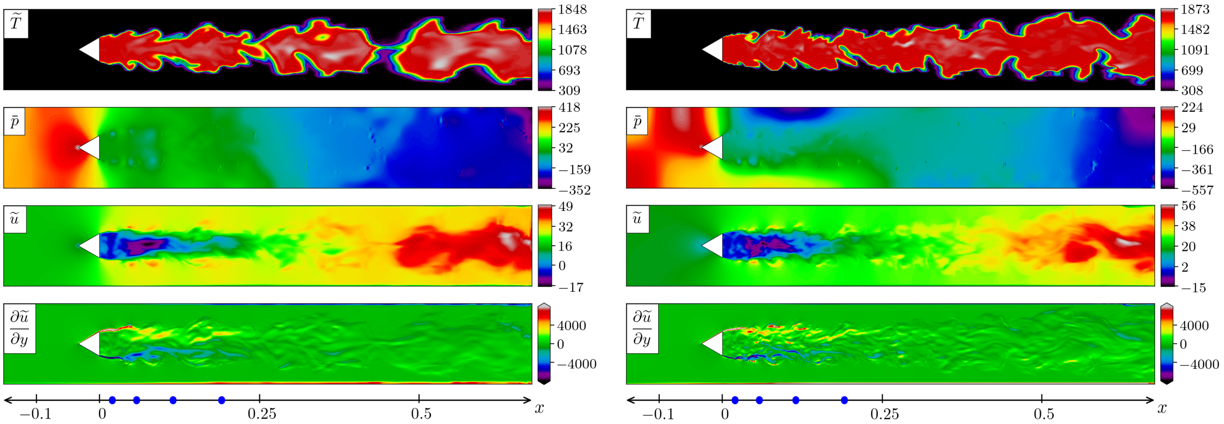

(a) *Coarse mesh.* (b) *Fine mesh.*

Figure 4.1: *Propane model contour plots. The field variables from top to bottom are temperature, gauge pressure, the horizontal velocity component and the y gradient of the horizontal velocity component.*

Results from both grids show that the flame has stabilized behind the flame holder and a recirculation zone has developed in the immediate wake region, as is evident by the blue and purple areas seen on the $\widetilde{u}$ contour plots. The recirculation zone lies in between the two shear layers that form as the flow separates from the upper and lower trailing edges of the flame holder. The shear layers are distinguished from elsewhere in the flow field by the large values of $\frac{\partial \widetilde{u}}{\partial y}$ that extend downstream of the flame holder to $x \approx 0.2$ m. The shear layers also mark the location of the flame front at the edge of the turbulent flame brush. As the oncoming unburnt mixture passes through the front, the gas is rapidly heated and it is drawn into the recirculation zone. The enhanced resolution of the fine grid reveals more of the smaller structures and instabilities of the flame, particularly along the outer edges of the flame brush where the gradients are better resolved.

A rotational velocity is induced on the flow once it separates from the flame holder, which gives rise to the Kelvin–Helmholtz instabilities [77] that are visible in both temperature plots. As the peaks of these wave–like structures collapse into the recirculation zone, they roll up into vortex sheets that enclose pockets of hot combustion products inside layers of cold reactants. This process continuously replenishes the recirculation zone with unburnt fuel that is promptly ignited.

Three–dimensional renders of the combustion chamber are given for each mesh in Figures 4.2 and 4.3. Figure 4.2 shows the turbulence intensity, as defined in Eq. (3.1), mapped onto iso–surfaces of the second invariant of the velocity gradient tensor [78]. The iso–surfaces represent turbulent structures that are characterised by regions of the flow where the fluid follows a specific vortical trajectory around the rotation axis of an elongated vortex core. Figure 4.3 shows the heat released through combustion. This is calculated as the volume integrated heat of combustion for a computational grid cell divided by the cell volume, $Q_\Delta = Q_{\text{cell}}/\Delta$.

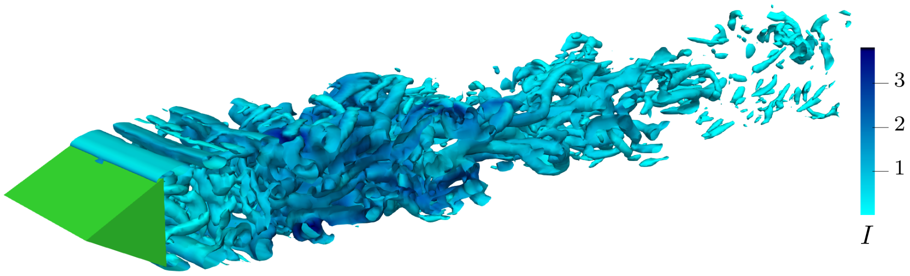

(a) *Coarse mesh.*

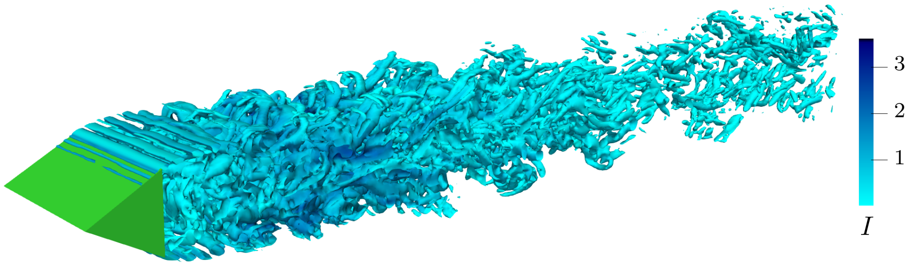

(b) *Fine mesh.*

Figure 4.2: *Propane model 3–D renders. Turbulence intensity mapped onto iso–surfaces of the second invariant of the velocity gradient tensor.*

Spanwise vortex structures that shed off the back of the flame holder can be seen in Figures 4.2a and 4.2b. Note that the upper and lower vortices rotate in opposite directions. In the middle of the recirculation zone these vortices both combine to direct the flow in the upstream direction, which then produces longitudinal vortex structures that are subsequently drawn downstream towards the outlet. The vorticity contributes to the viscous stresses acting on the fluid and intensifies the turbulence. The turbulence increases the flame speed, which boosts the consumption rate of the reactant species, leading to additional heat release and volumetric expansion.

Almost all of the heat release takes place along the outer edge of the turbulent flame brush inside the reaction zone of the flame front. The location of the flame front can be seen in Figure 4.3 where some distinctions are visible in the appearance of the flame given by the two different grids. The surface of the coarse grid flame is relatively smooth compared to that of the fine grid flame which shows a higher degree of surface wrinkling. This is because the chemical scales associated with the flame are only comparable to the smaller scales of the turbulence. By resolving a larger part of the inertial subregion (region II in Figure 2.3), the fine grid is able to capture the turbulence–chemistry interactions over a wider range of scales.

Smaller computational cells are needed to reveal eddies that can penetrate deeper into the flame front, modify its inner structure and enhance surface wrinkling. Many of these small eddies are filtered out of the coarse grid model, where the subgrid turbulent motions are modelled using instantaneous averages of the filtered velocity field. The visible distinction between the two flames in Figure 4.3 is explained by the existence these small–scale structures which are resolved with the fine grid but not with the coarse grid. As a result, only the interactions between large–scale structures and the flame are visible in Figure 4.3a. In Figure 4.3b the large–scale *and* the small–scale interactions can be seen. It is the high wavenumber eddies that strengthen the overall turbulence–chemistry interaction and give a more pronounced wrinkling effect.

The fine grid flame also shows localised regions of greater heat release compared to anywhere seen on the coarse grid flame, as the darker colours in Figure 4.3b suggest. Much of this can be attributed to the difference in grid resolution and the degree to which the TFM must increase the flame thickness so that it can be resolved on the grid. Because the coarse grid flame is thickened to a greater extent, the heat is released throughout a larger volume of space, as seen with the more diffuse looking flame in Figure 4.3a. In contrast, the fine grid flame is thinner and the heat release is concentrated within a smaller volume, as is evident by the crisp appearance of the flame in Figure 4.3a. Integrating Q_Δ across the entire domain gives a net heat release of $Q = 93.1$ $^{\mathrm{kJ}}/_{\mathrm{kg}}$ for the coarse grid. The net heat release for the fine grid is $Q = 102.5$ $^{\mathrm{kJ}}/_{\mathrm{kg}}$, which is approximately 9.5% higher. This is likely to be due to the greater level of turbulence–chemistry interaction that is achieved by the fine grid, which enhances the small–scale mixing process, increases the turbulent flame

(a) *Coarse mesh.*

(b) *Fine mesh.*

Figure 4.3: *Propane model 3–D renders. Heat release through combustion.*

speed and heightens the overall reaction rate.

Figure 4.4 features the Borghi diagram from Figure 2.8 and includes point data from the propane combustion model. The scatter points are coloured by the heat release to show where the reaction zone lies within the combustion regime. The values for s_L^0 and δ_L^0 were listed in Table 3.3. The turbulent velocity scale is calculated with Eq. (3.1), where it is assumed that $u_t = u'_{\text{rms}}$. The turbulent length scale is estimated as $\ell_t = 0.37(u_t^3/\varepsilon)$, which is given in the Fluent user documentation for premixed turbulent combustion models [50].

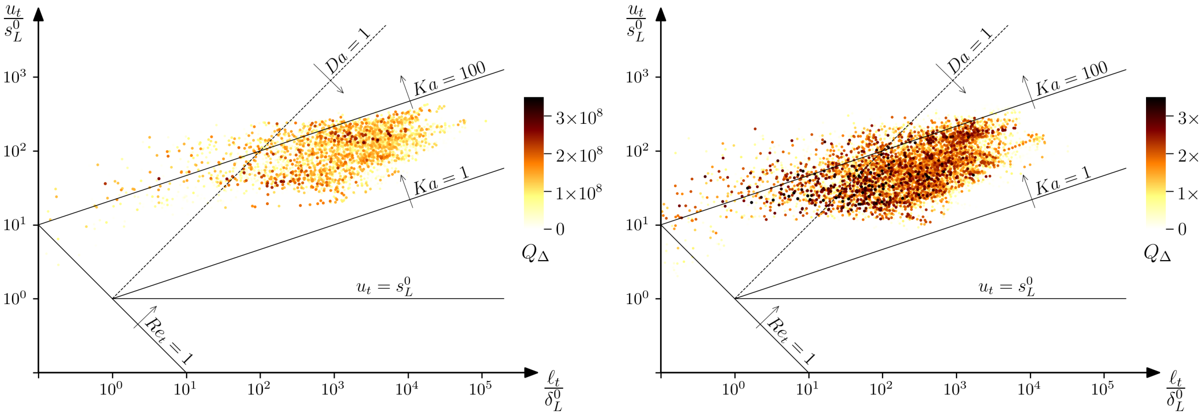

(a) *Coarse mesh.* (b) *Fine mesh.*

Figure 4.4: *Propane model Borghi diagram. The scatter points are coloured by the heat release.*

Figures 4.4a and 4.4b both show a high concentration of data points located around the same region of the graph, where the Damköhler and Karlovitz numbers are roughly on the order of $Da > 1$ and $1 < Ka < 100$. This indicates that the propane flame is predominantly within the thickened–wrinkled flame regime, which is in agreement with Fureby [79] and Zettervall et al. [80], who investigated similar cases of propane combustion.

The data distribution for the fine grid flame tends to be darker in colour and is shifted further towards the left hand side of the plot, where the Damköhler number is smaller and the Karlovitz number is larger. This reaffirms the previous discussion related to the nature of the flames in Figure 4.3. Recall that slightly more heat is released by the fine grid flame, which is assumed to be a result of the stronger turbulence–chemistry interaction. This is consistent with Figure 4.4b where there are considerably more scatter points located where $Da < 1$. Smaller values of Da correspond to more efficient mixing and an increased reaction rate. Consequently, more heat is released through combustion.

Figure 4.4 also helps to explain the difference in surface wrinkling between the two flames in Figure 4.3. The improved resolution of the fine grid is able to capture turbulent motions acting on scales small enough to disturb the inner reaction zone, modify its structure and enhance the wrinkling effect. This is expected to become an increasingly prominent feature of the flame dynamics once $Ka > 100$, which occurs to a greater extent in Figure 4.4b.

Figure 4.5 shows the selected species mass fractions of propane, carbon monoxide and water. The chemical transformations begin as soon as the unburnt mixture encounters the edge of the flame brush. As we have a lean fuel mix with $\phi = 0.65$, practically all of the propane is consumed within the reaction zone, leaving a burnt mixture that contains the excess oxygen mixed with hot combustion products. The drop in $\widetilde{Y}_{\mathrm{H_2}}$ and the corresponding rise in $\widetilde{Y}_{\mathrm{H_2O}}$ are consistent with the $\widetilde{T}$ gradient seen in Figure 4.1.

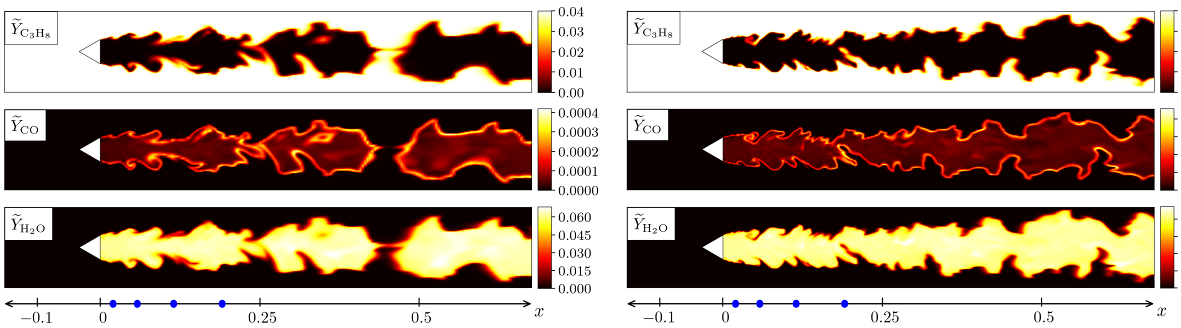

(a) *Coarse mesh.*

(b) *Fine mesh.*

Figure 4.5: *Propane model mass fractions. The chemical species from top to bottom are temperature propane, carbon monoxide and water.*

The reaction zone is seen as the bright strip that runs along the outer edge of the flame in the $\widetilde{Y}_{\mathrm{CO}}$ contour plots. Note that the reaction zones portrayed in Figure 4.5 have been artificially thickened and do not reflect the true thickness of premixed propane flames. As the only intermediate species to feature in the Ghani reaction mechanism, carbon monoxide typically has a brief existence compared to the other species. Carbon monoxide appears as a product species for the first step on the chemical pathway and as a reactant for the second step. We see the value of $\widetilde{Y}_{\mathrm{CO}}$ rapidly increases, before topping out and quickly dropping back down, in a similar fashion to the curve shown in Figure 2.5. Some CO molecules do not immediately participate in the second step of the chemical pathway and they instead manage to avoid destruction and exit the reaction zone intact. If any CO molecules do exit the reaction zone, the probability of their long–term survival is significantly increased. However, the burnt mixture contains leftover $\mathrm{O_2}$, so the two molecules can still encounter one another and complete the second step of the chemical pathway.

Figure 4.6 compares the time–averaged and RMS velocities from the propane combustion model to the experimental measurements obtained from the AFRL combustor [43]. While it should be noted that all experimental results are preliminary in nature and may be subject to revision, the data is considered to be reliable at present. For all plots in Figure 4.6, the CFD results for the coarse grid are plotted in blue, the CFD results for the fine grid are plotted in red and the ARFL measurements are plotted in black. The horizontal and vertical velocity components are given in Figures 4.6a and 4.6b, respectively. Velocities are normalised by the inlet flow velocity and the coordinates are normalised by the height of the flame holder. For reference, the location of the four profile stations from Figure 3.4 are indicated by the blue markers on the horizontal axis at the bottom of Figures 4.1 and 4.5.

The mean horizontal velocities in Figure 4.6a show very good agreement with experiment at stations closer to the flame holder. Above and below the recirculation zone, the results are good at all stations. However, the downstream recovery of $\langle\widetilde{u}\rangle$ between $y/h = \pm 0.6$ is overpredicted and the results become less accurate with increasing distance from the flame holder. This indicates that the length of the recirculation zone is shorter in the numerical model than it is in reality.

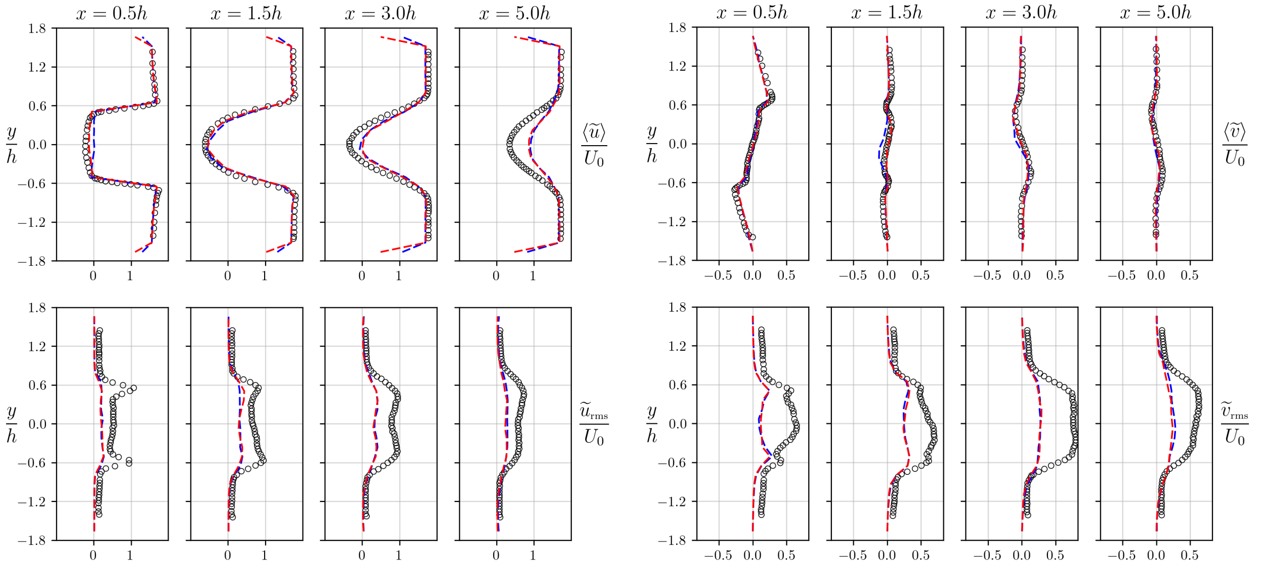

(a) *Axial velocity, $\widetilde{u}$.* (b) *Transverse velocity, $\widetilde{v}$.*

Figure 4.6: *Propane model filtered velocity profiles. The upper contour plots show the mean velocity profiles and the lower plots show the RMS velocity profiles. Velocity data is normalised by the inlet flow velocity $U_0 = 16.56$ m/s, and location coordinates are normalised by the flame holder height $h = 0.0381$ mm.*
Legend: --- *Coarse grid,* --- *Fine grid,* ∘∘∘∘ *AFRL measurements.*

Little difference is observed between the results obtained with the two grids. At $x = 0.5h$, the coarse mesh gives slightly larger values of $\langle\widetilde{u}\rangle$ near the centerline, but the two sets of results are much the same. The mean vertical velocities in Figure 4.6b also show good agreement with experiment. The coarse mesh shows a small deviation near the centerline at $x = 1.5h$ and $x = 3.0h$, but the results for the two grids otherwise give similar values for $\langle\widetilde{v}\rangle$.

The RMS velocities do not agree very well. Both $\widetilde{u}_{\mathrm{rms}}$ and $\widetilde{v}_{\mathrm{rms}}$ are underpredicted at every station. However, there are some small qualitative similarities. In some cases, the peaks that appear near the shear layers are somewhat visible, but they have no more than half of the amplitude that is observed in experiment.

A possible explanation for the discrepancy between the numerical and experimental results may be related to the particular reaction mechanism that was used. The chemical pathway in the Ghani mechanism contains just two elementary reactions. This likely ignores several relatively important chemical steps that occur when propane gas is burnt in practice. Many of these steps combine to form chain branching reactions that feature radical species with long residence times and can also include endothermic reactions. The volumetric expansion caused by the heat release has a stabilising effect on the vorticity that develops in the shear layers and will subsequently reduce the stresses acting on the flow inside the recirculation zone. Without a more realistic chemical pathway, the reacting gas will expand faster than it would in a physical system where it takes a longer time to break down the fuel. Therefore, the turbulence that is produced as expanding gas molecules are displaced, is dissipated prematurely and is not convected downstream. A shorter recirculation zone, lower downstream turbulence and poor RMS agreement in the shear layers, are all apparent from the velocity profiles in Figure 4.6.

4.2 Hydrogen Combustion

As stated in Section 3.4.2, the first hydrogen model gave nonsensical results and the computational domain had to be modified so that the flame was isolated from any false reflections caused by unphysical interactions between acoustic phenomena and the boundary conditions. A considerable amount of time was spent diagnosing the nature of the problem and testing alternative solutions. While extending the domain showed an immediate improvement in model performance it also increased the computing time required for processing the simulation. Consequently, a full set of sample data could not be collected within the allocated time frame and it was only feasible to model a single case of hydrogen combustion using the coarse grid. The hydrogen flame evolution is presented in Figures 4.7 and 4.8 as a sequence of instantaneous contour plots that illustrate the changes in time increments of 6.5 milliseconds. The sequence of five plots represent one complete flow–through of the combustion chamber with respect to the inlet flow velocity, $U_0 = 25.5008$ m/s. All other figures in the sections are from the final state of the simulation which is reached at approximately five complete flow–throughs after initialisation. Note that only the combustion chamber is of interest so the domain extensions are not pictured.

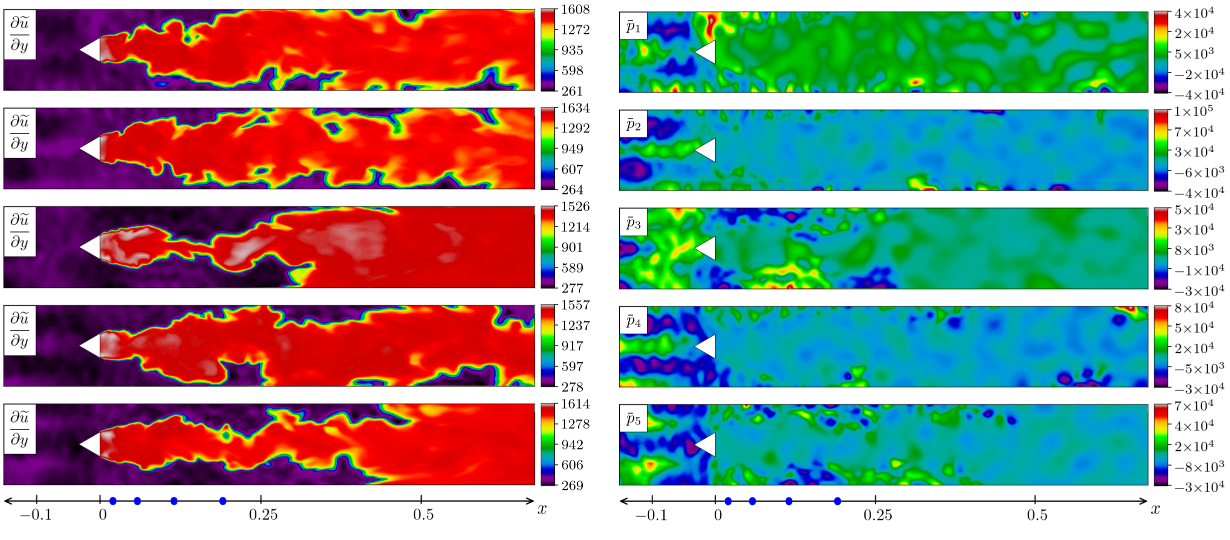

(a) *Temperture* (b) *Pressure*

Figure 4.7: *Evolution of the hydrogen flame temperature and pressure. Subscripts* 1 *to* 5 *each denote an additional time increment of* 6.5 *milliseconds.*

The $\widetilde{T}$ contour plots demonstrate the chaotic form of the hydrogen flame body, which appears to lack the consistency of the propane flame. The wave–like structures seen earlier in Figure 4.1 do not appear in any of the plots in Figure 4.7a and any orderly patterns that resemble Kelvin–Helmholtz billows are destroyed by the flames constant erratic motion. A consistent feature of the hydrogen flame is its tendency to expand vertically and touch the upper and lower combustor walls. Flame impingement is observed, to varying degrees, in every plot. Here, the nature of contact between the flame and the walls is not representative of a true physical system because the mechanics that describe flame–wall interactions were not included in the model. In reality the solid surfaces must facilitate some degree of heat flux. If heat is transferred from the flame to the wall due to large temperature gradients, the flame temperature rapidly decreases at the point of contact. Nearby chemical processes are deprived of the energy required to sustain a reaction which results in local flame extinction. This is known as *quenching*. In many combustion experiments the near–wall temperature gradients are large enough to quench the flame within micrometres of touching the wall, causing the reactions stop before contact can occur [37]. The solid surfaces in the CFD model are set as adiabatic boundaries and the effects of flame quenching are not taken into account.

The pressure field in Figure 4.7b also showcases the unsteadiness of the system. High frequency $\bar{p}$ waves that originate in the flame are seen propagating upstream of the flame holder, exiting through the inlet and into the forward extension duct of the domain. This is caused by thermo–acoustic instabilities which fluctuate in a resonant feedback mechanism. A key reason for the poor performance of the initial hydrogen model is likely due to the inability of the inlet and outlet boundaries to reconcile their prescribed configurations with these waves, which is known the cause major problems for boundary conditions [37].

The pressure waves induce fluctuations in the velocity field and the oscillations in $\widetilde{u}$ and $\frac{\partial \widetilde{u}}{\partial y}$ are clearly visible in Figure 4.8. The recirculation zone has developed between the upper and lower shear layers and is stable enough to keep the flame attached to the flame holder, although the tempestuous conditions restrict any sort of constancy to take shape.

Notice the sequence of changes seen in the velocity field from $\widetilde{u}_2$ to $\widetilde{u}_3$ to $\widetilde{u}_4$. The maximum and minimum velocities of $\widetilde{u}_3$ are notably different in comparison to those of $\widetilde{u}_2$ and $\widetilde{u}_4$. From $\widetilde{u}_2$ to $\widetilde{u}_3$ the bulk flow experiences an acceleration in the upstream direction before swinging back around towards the downstream

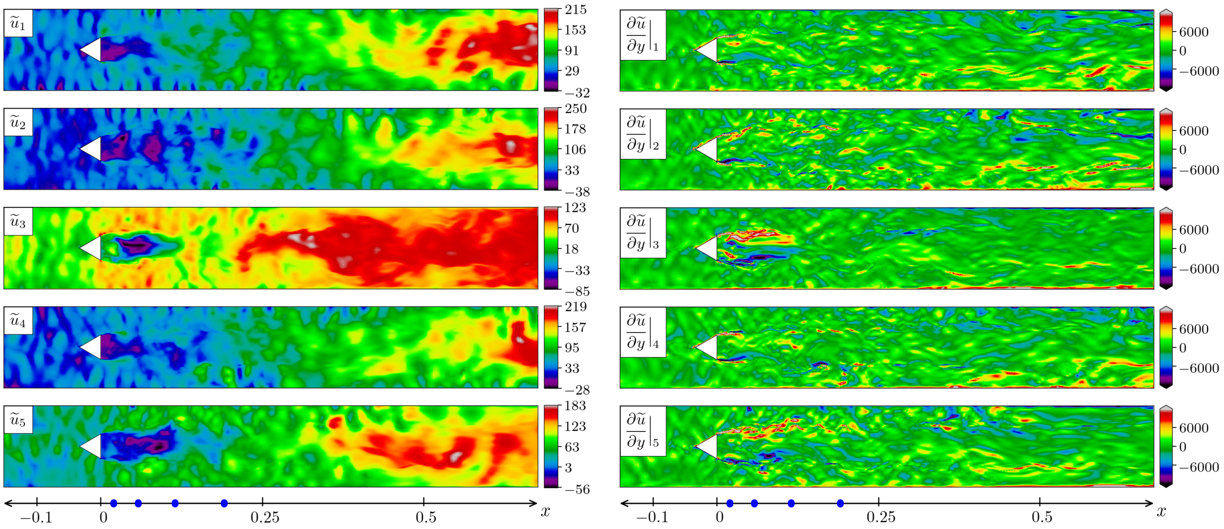

(a) *Horizontal velocity* (b) *Horizontal velocity gradient*

Figure 4.8: *Evolution of the hydrogen flame horizontal velocity and* y *gradient of the horizontal velocity. Subscripts* 1 *to* 5 *each denote an additional time increment of* 6.5 *milliseconds.*

direction at some stage between $\widetilde{u}_3$ and $\widetilde{u}_4$. The net effect is evident globally, which suggests that low frequency acoustics are also having an effect on the system dynamics. It appears that as a particular waveform propagates through the combustion chamber, $\widetilde{u}_3$ coincides with an instant in time where the phase angle is offset compared the original phase angle in $\widetilde{u}_2$. By the time we get to $\widetilde{u}_4$, one may suspect that roughly a full cycle, or possibly an integer product of multiple cycles, of this particular waveform is complete. It should be noted that conclusive statements about the precise nature of thermo–acoustic effects cannot be given much credibility without obtaining sufficient time series data for a comprehensive transient analysis.

Three–dimensional renders of the hydrogen model are given in Figure 4.9. The turbulence intensity of the hydrogen flame is shown in Figure 4.9a and is found to be up to three times higher than the turbulence intensity of the propane flame. The largest values of I tend to occur around the outer edges of the flame body, in contrast to the propane case where I was largest within the recirculation zone. In fact, the results show that the unburnt hydrogen mixture is generally more turbulent than the burnt mixture. This may explain the absence of clear and distinct vortex shedding at the flame holder trailing edges, an important feature of the propane flame. If the unburnt mixture is already highly turbulent by the time it passes the flame holder it would then interfere with the formation of well defined spanwise vortices, such as those seen in Figure 4.2. Any coherent vortical structures that arise when the flow separates at the trailing edge of the flame holder would presumably be destroyed just as quickly as they are created. It is conceivable that this also contributes to the overall destabilisation of the flame since the routine replenishment of unburnt reactants into the recirculation zone is far less consistent. In Figure 4.8a we can see how the recirculation zone struggles to maintain a steady form as it is relentlessly perturbed its highly dynamic surroundings.

The flow was found to be most turbulent well before it encounters the flame and ignites. The turbulence intensity approaches its maximum global value within the inlet extension duct prior to entering the combustion chamber. Recall that strong pressure wave are seen propagating upstream into this region and will induce turbulent fluctuations. Also note that the domain extensions feature much larger computational cells on account of the grid stretching. This calls into question the reliability of the values for I seen in Figure 4.9a. Because the upstream turbulence intensity is computed via the subgrid model across a region with large grid cells and is then convected into the combustion chamber, one should be somewhat sceptical before assuming that these number for I are physically valid.

Figure 4.9b shows the heat of combustion and the location of the hydrogen flame front. The extent of surface wrinkling appears to be on par with its propane counterpart in Figure 4.3a. As with the propane case, the lower resolution of the coarse grid is the limiting factor here and the flame would no doubt exhibit more wrinkling if it was modelled using a finer grid. The hydrogen flame has a somewhat diaphanous appearance in comparison to the propane flame. This is partly due to the colour and transparency effects used to render the

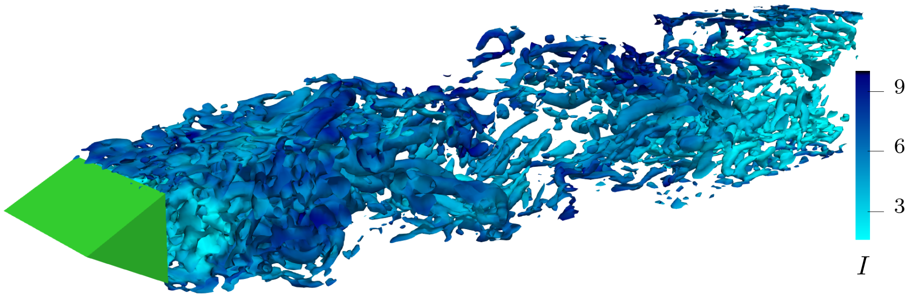

(a) *Turbulence intensity.*

(b) *Heat release.*

Figure 4.9: *Hydrogen model 3–D renders. Turbulence intensity and heat release through combustion.*

images, which are rescaled relative to Q_Δ. The key factor however, is the increased flame speed and decreased flame thickness, which result in hydrogen burning at a faster rate across a thinner reaction zone. Integrating Q_Δ across the entire combustion chamber gives the hydrogen flame a net heat release of $Q = 400.8\ \mathrm{kJ/kg}$, which is over four time greater than the propane flame.

Flame impingement on the upper and lower walls can be seen in Figure 4.9b where the flame abruptly disappears before it reaches the combustion chamber outlet. Any pockets of unburnt gas that are caught downstream from the point of contact are quickly consumed as the supply of fresh reactants is cut off. It is important to reiterate that any events directly related to wall contact are not physically valid here. Had flame–wall interactions been included in the model a certain degree of quenching would occur and flame impingement would be reduced, possibly even eliminated. This would be expected to have a considerable influence on the large–scale flame dynamics and overall evolution of the system.

Figure 4.10 shows the Borghi diagram for the hydrogen flame. It features a distribution of data points that are shifted upwards and further to the right hand side of the plot in comparison to the propane data seen in Figure 4.4. Most of the reaction zone is located inside the thickened—wrinkled flame combustion regime, although there are a fair number of areas that do fall within the thickened flame regime.

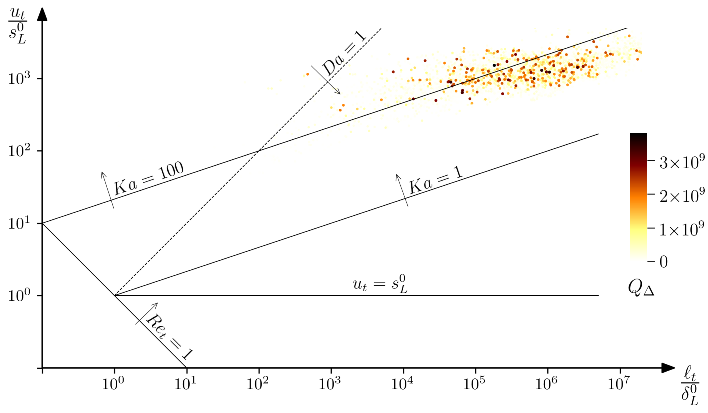

Figure 4.10: *Hydrogen model Borghi diagram. The scatter points are coloured by the heat release.*

It seems reasonable to suspect that a larger proportion of the flame may actually belong in the thickened flame regime where $Ka > 100$, due to the high level turbulence around the outer flame body. This would be the case if the turbulence intensity is accurate and sufficiently high to generate small–scale eddies capable of penetrating the relatively thin inner structure of the hydrogen flame with enough energy to modify the reaction zone and disturb the chemistry. But since the Karlovitz number is a measure of Kolmogorov scale interactions between turbulence and the flame, the resolution of the coarse grid is too low to capture such interactions.

The Damköhler number for the hydrogen flame is generally much smaller than is it for propane, indicating that the large–scale mixing process is more efficient here. Because the characteristic timescales of the largest eddies appears to be faster than the characteristic chemical timescales, the flame front is continuously replenished with fresh unburnt reactants faster than the combustion process can consume them. Therefore, the system may be considered to be approaching the state of a perfectly stirred reactor where $Da \ll 1$.

Figure 4.11 shows the selected species mass fractions of hydrogen, hydrogen peroxide, hydroperoxyl and water. The sequence of reactions featured in the Z22 reaction mechanism is triggered as soon as the unburnt gas encounters the flame front, at which point the H_2 species is rapidly consumed. A clear indication of where the reaction zone lies can be seen where there are large amounts of the short–lived H_2O_2. Notice the distinctive dot that lies behind the upper flame front just inside of the flame body, at $x \approx 0.2$ m. This small region contains a pocket of unburnt reactants that has been drawn into the flame by the turbulent conditions. It contains high concentrations of H_2 and H_2O_2 species, which under milder conditions would not have survived travelling this far into the interior of the flame body. Isolated unburnt regions like this have a high surface area to volume ratio. It allows them to persist for an extended with period of time because the unburnt species have poor exposure to their reaction partner species, delaying further chemical transformations.

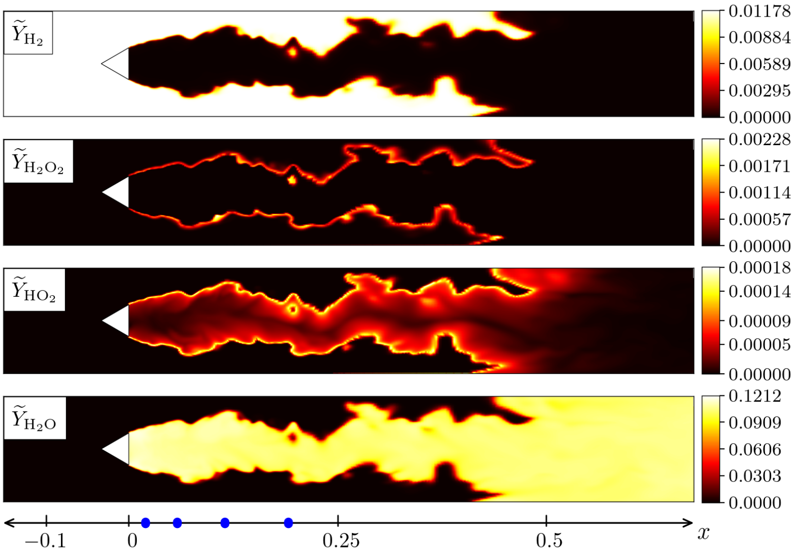

Figure 4.11: *Hydrogen model mass fractions. The chemical species from top to bottom are temperature hydrogen, hydrogen peroxide, hydroperoxyl and water.*

The HO_2 species is comparatively long–lived under these conditions and about half of the molecules that are produced at the front will survive the reaction zone and pass deeper into the flame body. In Figure 4.11 we can observe how the reduced number of reaction partners inside the flame body results in a longer residence time with the concentration of HO_2 showing a relatively gradual decline with increasing distance from the front. Although we see that practically all of the HO_2 is consumed by the time the gas exits the combustion chamber, it should be noted that flame impingement facilitates this to a certain degree. If the flame was not attached to the wall, the additional flame surface area would increase the production of HO_2, which would then result in higher concentrations passing through the outlet.

5 Concluding Remarks

It is difficult to draw definitive conclusions based on direct comparisons between the results from the propane and hydrogen combustion models. This is because the two systems ultimately behave very differently on a number of levels. The primary reason appears to be that combustion instabilities, which are present in the propane case, have a significantly larger influence on the overall system dynamics of the hydrogen case. While burning hydrogen was expected to produce stronger thermo–acoustic effects due to its unique reactive and diffusive properties, the extent to which these effects would overwhelmingly dominate the combustion process was not anticipated. Likewise, unexpected numerical problems were caused by the failure to accommodate the unsteadiness of the hydrogen flame and adapt the boundary conditions to the initial domain.

It is apparent that the approach used for switching fuels from propane to hydrogen that was described in Section 3.4 did not result in the two combustion cases sharing a great deal of dynamic characteristics. The absolute heat release was calculated a priori and used as a matching quantity. It was estimated to be $Q_{\text{abs}} = 337699$ W. The final values for absolute heat release are taken as the product of Q_{Δ} and $\dot{m}$ for their respective cases, and are listed in Table 5.1.

Fuel	C_3H_8	C_3H_8	H_2
Grid	Coarse	Fine	Coarse
Q_{abs} [W]	16933	18639	95699

Table 5.1: Absolute heat release.

In all cases the simulation results for Q_{abs} are much lower than the estimated value and there is a large discrepancy between the numbers for propane and hydrogen. The initial estimate was not expected to be highly accurate since it was calculated under the assumption of an idealised static system. Given the outcome of the simulations and the observations discussed above, it is unsurprising that the absolute heat release for hydrogen is larger than it is for propane. It may be possible to apply this approach to different cases and achieve results where the two types of fuel happen to burn in such a way that their combustion dynamics show a closer resemblance to one another. Perhaps matching up propane with another alkane type fuel that has similar physical and chemical properties, such as methane or butane, may yield better results.

One should consider that the particular system configuration that is specified for a given fuel may simply be incompatible with another type of fuel. In this thesis the propane model was based on the MVP workshop [41] specifications. Had an alternative system configuration been used for propane, say with a different equivalence ratio or mass flow rate, then the matching values for the hydrogen model would have also changed. This could go either way. The two models could converge towards a state in which many of their respective combustion dynamics are similar in nature. On the other hand, it could also result in global flame extinction for the seemingly matched case.

The approach of matching certain quantities could be further explored and modified by using other various system parameters of relevance. Non–dimensional quantities such as the Damköhler and Karlovitz numbers may be suitable for this type of analysis and were considered during the early phases of this thesis. However, the fact that Da and Ka are themselves dependant on turbulent quantities makes them very difficult to estimate without first obtaining reliable sample data from a non-reactive CFD model. In the case of hydrogen combustion, based on the observed sensitivity of the flame to combustion instabilities, it may be worthwhile conducting a preliminary analysis into the effects of thermo–acoustic phenomena. Although much could be learnt from such an approach it would be a very challenging endeavour. Especially without a complimentary empirical study to provide reliable validation data. Poinsot and Veynante [37] emphasise that "there is no reliable method to predict the occurrence and characteristics of combustion instabilities without first firing up the combustor".

Putting aside the means used to decide the initial system configuration, there are several ways in which the present study could be improved or extended. The propane case would certainly benefit from a more comprehensive reaction mechanism. During the early stages of the project an additional model for propane combustion that used the skeletal Z66 mechanism [80] was considered. Z66 features twenty–five chemical species and sixty–six elementary reaction, which provides a far more complete description of the chemical processes that occur when propane is burnt. However, this was found to be too computationally expensive and would detract from the primary goal of modelling hydrogen combustion.

Acoustic waves generated by the flame could be investigate using dynamic mode decomposition [81]. This was initially included in the set of objectives for this thesis and would have likely provided insight into the effects of combustion instabilities. Dynamic mode decomposition requires time series data, which could not be collected for the hydrogen case, and a decision was ultimately made not to include it in the analysis. The issue of flame impingement should also be addressed it is expected to occur under certain conditions. This would require configuring the walls of the combustion chamber with appropriate boundary conditions which allow for the correct amount heat transfer that the thermal conductivity of the wall material provides. In practice, the temperature of combustor walls is controlled and they typically experience a heat flux of about 1 $^{\mathrm{MW}}/_{\mathrm{m}^2}$ [37].

On a positive note, it has been verified that CFD models of propane combustion can be constructed and used to predict certain aspects of the combustions dynamics to a fair degree of accuracy. Furthermore, the capability for using CFD to simulate a working hydrogen flame has been demonstrated. Most of all, this study showcases the challenges associated with such a task and shines light on some of the key issues that may arise when carrying out such an investigation. The adoption of hydrogen as a primary source of fuel is certainly achievable. It is hoped that the knowledge gained throughout this thesis will contribute towards the next step in the path that brings us to a full–fledged hydrogen economy.

References

[1] J. Haldane. *Daedalus: Or, Science and the Future; a Paper Read to the Heretics.* K. Paul, Trench, Trubner & Company, Limited, 1923.

[2] L. W. Jones. *Toward a Liquid Hydrogen Fuel Economy.* University of Michigan, Mar. 1970.

[3] J. O. M. Bockris. The Hydrogen Economy: Its History. *International Journal of Hydrogen Energy* **38**.6 (Feb. 2013), 2579–2588. DOI: `10.1016/j.ijhydene.2012.12.026`.

[4] "Australia's National Hydrogen Strategy". Department of Industry, Innovation and Science, Canberra. 2019. URL: `https://www.industry.gov.au/sites/default/files/2019-11/australias-national-hydrogen-strategy.pdf`.

[5] "A Hydrogen Strategy for a Climate–Neutral Europe". European Commission, Brussels. 2020. URL: `https://ec.europa.eu/energy/sites/ener/files/hydrogen_strategy.pdf`.

[6] "The National Hydrogen Strategy". Federal Ministry for Economic Affairs and Energy, Berlin. 2020. URL: `https://www.bmwi.de/Redaktion/EN/Publikationen/Energie/the-national-hydrogen-strategy.pdf`.

[7] "The Basic Hydrogen Strategy". Ministry of Economy, Trade and Industry, Tokyo. 2017. URL: `https://www.meti.go.jp/english/press/2017/pdf/1226_003b.pdf`.

[8] "National Hydrogen Energy Roadmap". Department of Energy, Washington. 2002. URL: `https://www.hydrogen.energy.gov/pdfs/national_h2_roadmap.pdf`.

[9] P. Chiesa, G. Lozza and L. Mazzocchi. Using Hydrogen as Gas Turbine Fuel. *Journal of Engineering for Gas Turbines and Power* **127**.1 (Feb. 2005), 73–80. DOI: `10.1115/1.1787513`.

[10] M. Nose et al. Hydrogen–Fired Gas Turbine Targeting Realization of CO2–Free Society. *Mitsubishi Heavy Industries Technical Review* **55**.4 (Dec. 2018), 1–7.

[11] "Hydrogen Gas Turbines: The Path Towards A Zero–Carbon Gas Turbine". ETN Global, Brussels. 2020. URL: `https://etn.global/wp-content/uploads/2020/02/ETN-Hydrogen-Gas-Turbines-report.pdf`.

[12] "Power to Gas: Hydrogen for Power Generation". GE Power, Atlanta. 2019. URL: `https://www.ge.com/power/gas/fuel-capability/hydrogen-fueled-gas-turbines`.

[13] J. Sosa et al. Experimental Evidence of H2/O2 Propellants Powered Rotating Detonation Waves. *Combustion and Flame* **214** (Apr. 2020), 136–138. DOI: `10.1016/j.combustflame.2019.12.031`.

[14] G. Choubey et al. Hydrogen Fuel in Scramjet Engines – A Brief Review. *International Journal of Hydrogen Energy* **45** (June 2020), 16799–16815. DOI: `10.1016/j.ijhydene.2020.04.086`.

[15] F. Calise et al. *Solar Hydrogen Production: Processes, Systems and Technologies.* Academic Press, 2019. ISBN: 9780128148549.

[16] H. Xiao et al. Experimental Study on the Behaviors and Shape Changes of Premixed Hydrogen–Air Flames Propagating in Horizontal Duct. *International Journal of Hydrogen energy* **36** (Mar. 2011), 6325–6336. DOI: `10.1016/j.ijhydene.2011.02.049`.

[17] B. E. Gelfand et al. *Thermo–Gas Dynamics of Hydrogen Combustion and Explosion.* Springer, 2012. ISBN: 9783642253522.

[18] E. L. Cussler and E. L. Cussler. *Diffusion: Mass Transfer in Fluid Systems.* Cambridge University Press, 2009. ISBN: 9780521871211.

[19] C. K. Law. Combustion at a Crossroads: Status and Prospects. *Proceedings of the Combustion Institute* **31** (Jan. 2007), 1–29. DOI: `10.1016/j.proci.2006.08.124`.

[20] M. Ó Conaire et al. A Comprehensive Modeling Study of Hydrogen Oxidation. *International Journal of Chemical Kinetics* **36** (Aug. 2004), 603–622. DOI: `10.1002/kin.20036`.

[21] A. L. Sánchez and F. A. Williams. Recent Advances in Understanding of Flammability Characteristics of Hydrogen. *Progress in Energy and Combustion Science* **41** (Apr. 2014), 1–55. DOI: `10.1016/j.pecs.2013.10.002`.

[22] A. A. Konnov. Remaining Uncertainties in the Kinetic Mechanism of Hydrogen Combustion. *Combustion and Flame* **152** (Mar. 2008), 507–528. DOI: `10.1016/j.pecs.2013.10.002`.

[23] "World Energy Balances 2019". IEA, Paris. 2019. ISBN: 9789264318922.

[24] C. Darwin. *The Descent of Man and Selection in Relation to Sex.* Vol. 1. D. Appleton, 1896.

[25] A. Cohen et al. The Global Burden of Disease Due to Outdoor Air Pollution. *Journal of Toxicology and Environmental Health, Part A* **68** (Sept. 2005), 1301–1307. DOI: `10.1080/15287390590936166`.

[26] "Global Health Risks: Mortality and Burden of Disease Attributable to Selected Major Risks". World Health Organisation, Geneva. 2009. URL: `https://www.who.int/healthinfo/global_burden_disease/GlobalHealthRisks_report_full.pdf`.

[27] J. Cook et al. Quantifying the Consensus on Anthropogenic Global Warming in the Scientific Literature. *Environmental Research Letters* **8** (May 2013), 024024. DOI: `10.1088/1748-9326/8/2/024024`.

[28] N. Oreskes. The Scientific Consensus on Climate Change. *Science* **306** (Dec. 2004), 1686–1686. DOI: `10.1126/science.1103618`.

[29] W. R. Anderegg et al. Expert Credibility in Climate Change. *Proceedings of the National Academy of Sciences* **107** (July 2010), 12107–12109. DOI: `10.1073/pnas.1003187107`.

[30] R. C. Flagan and J. H. Seinfeld. *Fundamentals of Air Pollution Engineering.* Courier Corporation, 2012. ISBN: 9780486488721.

[31] P. S. Nigam and A. Singh. Production of Liquid Biofuels from Renewable Resources. *Progress in Energy and Combustion Science* **37**.1 (Feb. 2011), 52–68. DOI: `10.1016/j.pecs.2010.01.003`.

[32] B. Zohuri. *Hydrogen Energy: Challenges and Solutions for a Cleaner Future.* Springer, 2018. ISBN: 9783319934600.

[33] A. Date. *Analytic Combustion: With Thermodynamics, Chemical Kinetics and Mass Transfer.* 2nd ed. Cambridge University Press, 2011. ISBN: 9781139499071.

[34] T. Tao. *Kolmogorov's Power Law for Turbulence.* Available at `https://terrytao.wordpress.com/` (2020/05/28).

[35] P. Bradshaw. The Understanding and Prediction of Turbulent Flow. *The Aeronautical Journal* **76**.739 (July 1972), 403–418. DOI: `10.1017/S0001924000043360`.

[36] L. da Vinci. *Studies of Water.* Available at `https://www.rct.uk/` (2020/05/27).

[37] T. Poinsot and D. Veynante. *Theoretical and Numerical Combustion.* 3rd ed. 2012. ISBN: 9782746639904.

[38] B. T. Paxton et al. "Development and Characterization of an Experimental Arrangement for Studying Bluff–Body-Stabilized Turbulent Premixed Propane–Air Flames". AIAA Scitech 2019 Forum (San Diego, USA, Jan. 7–June 11, 2019), p. 0118. DOI: `10.2514/6.2019-0118`.

[39] W. Kim and S. Menon. "A New Dynamic One–Equation Subgrid–Scale Model for Large Eddy Simulations". 33rd Aerospace Sciences Meeting and Exhibit (Reno, USA, Jan. 9–12, 1995). DOI: `10.2514/6.1995-356`.

[40] O. Colin et al. A Thickened Flame Model for Large Eddy Simulations of Turbulent Premixed Combustion. *Physics of Fluids* **12**.7 (June 2000), 1843–1863. DOI: `10.1063/1.870436`.

[41] "4th Model Validation for Propulsion Workshop". AIAA SciTech Forum and Exposition (Orlando, USA, Jan. 7–9, 2020). URL: `https://community.apan.org/wg/afrlcg/mvpws`.

[42] A. Ghani et al. LES of Longitudinal and Transverse Self–Excited Combustion Instabilities in a Bluff–Body Stabilized Turbulent Premixed Flame. *Combustion and Flame* **162**.11 (Nov. 2015), 4075–4083. DOI: `10.1016/j.combustflame.2015.08.024`.

[43] C. A. Fugger et al. "Measurements and Analysis of Flow–Flame Interactions in Bluff–Body–Stabilized Turbulent Premixed Propane–Air Flames". AIAA SciTech 2019 Forum (San Diego, USA, Jan. 7–June 11, 2019). DOI: `10.2514/6.2019-0453`.

[44] C. Fureby. "A Large Eddy Simulation (LES) Study of the VOLVO and AFRL Bluff Body Combustors at Different Operating Conditions". AIAA SciTech 2019 Forum (San Diego, USA, Jan. 7–June 11, 2019). DOI: `10.2514/6.2019-0453`.

[45] N. Zettervall and C. Fureby. "A Computational Study of Ramjet, Scramjet and Dual–Mode Ramjet Combustion in a Combustor with a Cavity Flameholder". 2018 AIAA Aerospace Sciences Meeting (Kissimmee, USA, Jan. 8–12, 2018). DOI: `10.2514/6.2018-1146`.

[46] W. Waidmann et al. Supersonic Combustion of Hydrogen/Air in a Scramjet Combustion Chamber. *Space Technology* **6**.15 (1995), 421–429.

[47] C. Fureby. "A Comparative Study of Subgrid Models, Reaction Mechanisms and Combustion Models in LES of Supersonic Combustion". AIAA Propulsion and Energy 2019 Forum (Indianapolis, USA, Aug. 19–22, 2019). DOI: `10.2514/6.2019-4273`.

[48] A. Lipatnikov. *Fundamentals of Premixed Turbulent Combustion.* CRC Press, 2012. ISBN: 9781466510241.

[49] L. Boltzmann. *Lectures on Gas Theory.* Dover Books on Physics. Dover Publications, 2012. ISBN: 9780486152332.

[50] ANSYS Fluent, 19.0, User's Guide/Theory Guide. *ANSYS Inc., Canonsburg, USA* (2019).

[51] S. Chapman and T. G. Cowling. *The Mathematical Theory of Non–uniform Gases.* 2nd ed. Cambridge University Press, 1953. ISBN: 9780521408448.

[52] B. J. McBride, S. Gordon and M. A. Reno. *Coefficients for Calculating Thermodynamic and Transport Properties of Individual Species.* National Aeronautics and Space Administration, 1993. ISBN: 9781722303716.

[53] D. Oxtoby, H. P. Gillis and A. Campion. *Principles of Modern Chemistry.* 7th ed. Cengage Learning, 2011. ISBN: 9780840049315.

[54] I. Müller. *A History of Thermodynamics: The Doctrine of Energy and Entropy.* Springer, 2007. ISBN: 9783540462279.

[55] F. Williams. *Combustion Theory.* CRC Press, 2018. ISBN: 9780429973680.

[56] R. A. Alberty. Use of Legendre Transforms in Chemical Thermodynamics (IUPAC Technical Report). *Pure and Applied Chemistry* **73** (Aug. 2001), 1349–1380.

[57] K. K. Kuo. *Principles of Combustion.* 2nd ed. Wiley, 2005. ISBN: 0471046892.

[58] S. B. Pope. *Turbulent Flows.* Cambridge University Press, 2000. ISBN: 9780521591256.

[59] A. N. Kolmogorov. Dissipation of Energy in Locally Isotropic Turbulence. *Akademiia Nauk SSSR Doklady* **32** (Apr. 1941), 16–18.

[60] E. Garnier, N. Adams and P. Sagaut. *Large Eddy Simulation for Compressible Flows.* Springer Science & Business Media, 2009. ISBN: 978-90-481-2818-1.

[61] S. De et al. *Modeling and Simulation of Turbulent Combustion.* Springer, 2018. ISBN: 9789811074103.

[62] S.-E. Kim. “Large Eddy Simulation Using an Unstructured Mesh Based Finite–Volume Solver”. 34th AIAA fluid dynamics conference and exhibit (Portland, USA, June 28–Jan. 7, 2004). DOI: `10.2514/6.2004-2548`.

[63] S. Turns. *An Introduction to Combustion: Concepts and Applications.* 3rd ed. McGraw-Hill International, 2012. ISBN: 9780073380193.

[64] N. Peters. *Turbulent Combustion.* Cambridge University Press, 2000. ISBN: 9781139428064.

[65] K. Kuo and R. Acharya. *Fundamentals of Turbulent and Multiphase Combustion.* Wiley, 2012. ISBN: 9781118099292.

[66] F. Gouldin. “Combustion Intensity and Burning Rate Integral of Premixed Flames”. Symposium (International) on Combustion. Vol. 26. 1. Elsevier. 1996, pp. 381–388. DOI: `10.1016/S0082-0784(96)80239-6`.

[67] G. Damköhler. The Effect of Turbulence on the Flame Velocity in Gas Mixtures. *Journal for Electrochemistry and Applied Physical Chemistry* **46**.11 (1940), 601–626.

[68] R. Borghi. “On the Structure and Morphology of Turbulent Premixed Flames”. *Recent advances in the Aerospace Sciences.* Springer, 1985, pp. 117–138. ISBN: 978-1-4684-4300-4.

[69] G. Wang, M. Boileau and D. Veynante. Implementation of a Dynamic Thickened Flame Model for Large Eddy Simulations of Turbulent Premixed Combustion. *Combustion and Flame* **158**.11 (2011), 2199–2213. DOI: `10.1016/j.combustflame.2011.04.008`.

[70] P. Siemens. Simcenter STAR–CCM+ User Guide V13. 04. *CD-Adapco: New York, USA* (2018).

[71] R. J. Kee, F. M. Rupley and J. A. Miller. *Chemkin–II: A Fortran Chemical Kinetics Package for the Analysis of Gas–Phase Chemical Kinetics.* Tech. rep. Sandia National Laboratries, Livermore, USA, 1989.

[72] R. Design. ANSYS CHEMKIN Theory Manual 17.0. *San Diego, USA* (2017).

[73] D. G. Goodwin et al. *Cantera: An Object–oriented Software Toolkit for Chemical Kinetics, Thermodynamics, and Transport Processes.* `https://www.cantera.org`. Version 2.4.0. 2018. DOI: `10.5281/zenodo.1174508`.

[74] B. E. Launder and D. B. Spalding. *Lectures in Mathematical Models of Turbulence.* Academic press, 1972. ISBN: 0124380506.

[75] B. Magnussen. “On the Structure of Turbulence and a Generalized Eddy Dissipation Concept for Chemical Reaction in Turbulent Flow”. 1981 AIAA Aerospace Sciences Meeting (St. Louis, USA, Jan. 12–15, 1981). DOI: `10.2514/6.1981-42`.

[76] R. I. Issa. Solution of the Implicitly Discretised Fluid Flow Equations by Operator-Splitting. *Journal of Computational Physics* **62** (Jan. 1986), 40–65. DOI: `10.1016/0021-9991(86)90099-9`.

[77] W. Thomson Baron Kelvin. XLVI. Hydrokinetic Solutions and Observations. *The London, Edinburgh, and Dublin Philosophical Magazine and Journal of Science* **42**.281 (1871), 362–377. DOI: `doi.org/10.1080/14786447108640585`.

[78] J. Jeong and F. Hussain. On the Identification of a Vortex. *Journal of Fluid Mechanics* **285** (Feb. 1995), 69–94. DOI: `10.1017/S0022112095000462`.

[79] C. Fureby. “A Comparative Study of Large Eddy Simulation (LES) Combustion Models Applied to the Volvo Validation Rig”. 55th AIAA Aerospace Sciences Meeting (Grapevine, USA, Jan. 9–13, 2017). DOI: `10.2514/6.2017-1575`.

[80] N. Zettervall et al. Large Eddy Simulation of a Premixed Bluff Body Stabilized Flame Using Global and Skeletal Reaction Mechanisms. *Combustion and Flame* **179** (May 2017), 1–22. DOI: `10.1016/j.combustflame.2016.12.007`.

[81] P. J. Schmid. Dynamic Mode Decomposition of Numerical and Experimental Data. *Journal of Fluid Mechanics* **656** (Aug. 2010), 5–28. DOI: `10.1017/S0022112010001217`.